

A Minimal Network of Brain Dynamics: Hierarchy of Approximations to Quasi-critical Neural Network Dynamics

Jeremy B. Goetz,^{1,*} Naruepon Weerawongphrom,^{1,*}

Rashid V. Williams-García,² John M. Beggs,¹ and Gerardo Ortiz¹

¹*Department of Physics, Indiana University, Bloomington, Indiana 47405, USA*

²*Institut Denis Poisson, Parc de Grandmont, Tours 37200 FRANCE*

(Dated: December 29, 2025)

We present an interacting branching model of neural network dynamics, incorporating key biological features such as inhibition with several types of inhibitory interactions. We establish a hierarchy of analytical mean-field approximations to the model, which characterizes nonequilibrium phase transitions between disorder and ordered phases, and perform a stability analysis. Generically, inhibitory neurons increase the stability of the model dynamics. The model is consistent with the quasi-criticality hypothesis in that it displays regions of maximal dynamical susceptibility and maximal mutual information predicated on the strength of the external stimuli. Directed percolation emerges as the universality class of the critical transition of the model, consistent with some previous experimental data and models. In the unstable phase, chaotic dynamics emerge, which may be linked to the occurrence of epileptic seizures.

I. INTRODUCTION

The human brain is a highly intricate open system with nonequilibrium stochastic dynamics, numerous neurotransmitters, and hundreds of different types of neurons. In total, it is estimated that there are 20×10^9 neurons with 150×10^{12} connections in the neocortex [1, 2]. The cortex is the most evolutionarily recent component of mammalian brains, and is thought to be responsible for higher cognition, as well as sensory and motor functions [3]. Given its importance, researchers have developed numerous biological neural network models to study the cortex. These models typically employ continuous partial differential equations or discrete cellular automata. These models often fall into two categories: highly detailed models that are not analytically tractable, and simplified models —such as mean-field (MF) approximations— that are analytically tractable but whose dynamics are reduced to the extent that they can no longer capture spatiotemporal patterns, such as avalanches—bursts of activity separated by quiescent periods— commonly observed in experiments. One of the commonly neglected components are inhibitory neurons, which make up approximately 20% of all neurons in the cortex [4]. Inhibitory neurons are thought to ensure stable dynamics while networks perform complex processing tasks [5].

The seminal work of Wilson and Cowan serves as the foundation of many modern models that include inhibitory neurons [6]. A limitation of this model in its MF form is its inability to capture spatiotemporal dynamics such as avalanches. To address this, researchers have developed branching process-like models [7–12]. One popular model from this class is the Cortical Branching Model (CBM) [13], which featured avalanche dynamics

and an analytically tractable dynamical MF approximation, however, it was crucially missing inhibitory neurons. A notable example of a model incorporating inhibitory neurons was introduced in [14], which developed a critical continuous branching process (contact process) model that focused on inhibitory-dominated networks that show rich phase diagrams. However, this is a rate model and is, thus, unable to simulate experimental avalanches, in addition to lacking neuronal refractory periods.

This paper aims to build a model that addresses these common shortcomings and matches the current experimental data. We will now describe two key aspects of the data we aim to model: (1) that living neuronal networks show many signatures of operating near criticality, and (2) that these networks are not actually critical, but quasi-critical.

Regarding operating near criticality, we begin with well-established experimental observations of neuronal avalanches, which exhibit seemingly scale-free distributions of avalanche sizes and durations, consistent exponent scaling relationships, and universal scaling functions (i.e., shape collapse) [15–20]. Scale-free properties confer optimal information processing, such as divergent dynamical susceptibility, maximal mutual information, maximal computational power, etc., and are expected to characterize universal behavior [13, 21, 22]. Exponent scaling relations have been shown to hold for experiments performed with anesthetized rats, monkeys, freely-moving mice, and *ex vivo* turtles [23]. However, these experiments also show different critical exponents for the same animal at different times, indicating that while neuronal activity is approximately critical, it is not necessarily universal [15, 20, 24–26].

Regarding quasi-criticality, this lack of expected universality is but one observation demonstrating that these networks are not actually critical. They are also of finite size and constantly driven by inputs from other areas of the brain. The net effect is that singularities repre-

* These authors contributed equally.

senting phase transitions are smeared and shifted [27]. Together, these facts indicate that the cortex cannot be truly critical. One alternative to the criticality hypothesis is the quasi-criticality hypothesis, which embraces the scaling theory of phase transitions and has been recently proposed as an organizing principle for brain dynamics. According to the quasi-criticality hypothesis, the cortex operates in a region of functional parameters close to a surface of maximal dynamical susceptibility and maximal mutual information (the nonequilibrium Widom line) which depends on the strength of the external drive [13]. It has been confirmed experimentally and by simulations that quasi-criticality can account for an *effective* scaling-law behavior [17], allowing us to measure how much the dynamics depart from that effective scaling regime [13, 17]. If the cortex follows the principles of quasi-criticality, a minimalist model can encapsulate the fundamental features of the corresponding emergent phenomena.

To build on the experimental and theoretical evidence of quasi-criticality, we introduce the Generalized Cortical Branching Model (GCBM), an extension of the Cortical Branching Model (CBM) that includes inhibition. The objective of the GCBM is to capture the essentials of neural dynamics with minimal features, increasing the predictive power of the quasi-criticality hypothesis. Also, including inhibitory neurons in the GCBM allows the model to be tuned in various ways to move the system towards or away from the quasi-critical region. This allows the model to test a wider range of dynamics and provides potential insight into how and why the cortex adjusts its proximity to the quasi-critical region. The GCBM is a functional network closely related to a nonequilibrium stochastic cellular automaton without a regular grid as the spatial structure or an inherent distance metric between cells. GCBM is a many-body simulator that tracks the state of each neuron (quiescent, active, or refractory) and the propagation of activity between neurons. To find an in-depth analysis of the GCBM many-body simulator, please refer to this paper [28].

There are limitations to fundamental discoveries with the many-body simulations since they fall within the non-deterministic polynomial time (NP) class of problems, exponentially dependent on the number of neurons, with solutions that are not analytical or tractable, and a surplus of data and parameters of the model. To circumvent this issue, in this paper we employ a hierarchy of MF approximations which are analytically tractable. This leads to a reduction in dimensionality in which the system is described by a coupled, autonomous, nonlinear discrete dynamical map of first order, with dimensionality set by the integer-valued refractory periods. More fundamentally, this dimensionality reduction method through MF approximations applies to functional networks in general, where this paper is an application of this methodology. We perform dimensionality reduction by representing different hierarchies of neuronal networks by network motifs. A motif could be a simple connectivity pattern

between excitatory and inhibitory neurons, for example. When such a motif is replicated and translated, it can generate a larger complex network in the same way that a simple tile, when tessellated, can cover a large plane. These motifs are therefore the fundamental components needed to recreate the network by replication and translation. Given these simple motifs, MF equations can be derived, using a systematic *dictionary* supplemented by basic substitution rules, to represent the dynamics. Although not as systematic as the work presented here, the initial groundwork for incorporating inhibitory neurons into the MF framework was laid out in Mark Moore's thesis [29].

These MF equations allow for the examination of the roles of inhibitory neurons in modulating the dynamics and assessing the model's consistency with the quasi-criticality hypothesis. As we will see, the inclusion of inhibitory neurons increases the system's stability by shifting the phase boundaries to more stable regions, also reducing the peak susceptibility as the strength of inhibition increases, which are experimentally testable prediction. We observe a second-order phase transition between disordered and ordered regimes, marked by a peak in susceptibility at the critical point where spontaneous activity is absent—behavior consistent with purely excitatory models and supporting the quasi-criticality hypothesis. Notably, in the absence of spontaneous activity, the model falls within the directed percolation universality class, in agreement with the excitatory-only CBM. We also characterize the previously labeled quasiperiodic phase as marginally stable, leading to a period-doubling route to chaos. The transitions through marginally stable, periodic orbits, and the period-doubling route to chaos can be related to epileptic seizures as explored in chaos theory and neural dynamics studies [30–33].

The rest of this paper is organized as follows: Starting with Section II, we show the equations of the many-body GCBM to derive the MF approximations. Section III provides the steps for developing the Hierarchy of MF approximations, which enables a concise method for writing solutions for every motif. Section IV provides examples of how to solve MF equations for a simple and a complex network. In Section V, we will analyze how adding inhibitory neurons affects the dynamics, analyze phase diagrams, compute the dynamical susceptibility with variations of inhibitory strengths, discuss the universality class of the model for no external driver, the physical and non-physical chaotic regimes of the model, discuss paths to chaos, and explore forcing inhibitory neurons to be periodic and its effect on excitatory neurons. We conclude in Section VI with a summary of the main results, where we highlight the central findings and their implications. A notation guide can be found in Appendix A, where terms are organized by order of appearance.

II. GENERALIZED CORTICAL BRANCHING MODEL

A. Branching dynamics

The GCBM simulates biological spiking activity using a branching process model. Briefly, this model consists of nodes (neurons), connected to other nodes in a network that can fire in response to inputs. Unlike leaky integrate and fire models that are common in computational neuroscience, this model does not have nonlinear thresholds for its neurons. Rather, the neurons will fire if they receive net positive inputs and they are not in the refractory state.

We will now describe the model in more detail. The model consists of excitatory and inhibitory neurons, located at the node or vertex of the network, labeled e and i , respectively, while $n \in \{e, i\}$ denotes a generic neuron. The total number of neurons is given by $N = N_e + N_i$, where N_e and N_i denote the numbers of excitatory and inhibitory neurons, respectively. Excitatory and inhibitory neurons are labeled by e_μ and i_ν where index $\mu = 1, \dots, N_e$ and $\nu = 1, \dots, N_i$. The subscripts μ, ν are used to distinguish excitatory and inhibitory neurons, respectively.

Neurons are connected via fixed transmission channels. All neurons start in a resting state but can become active spontaneously or due to signals from presynaptic neighbors. Active neurons propagate signals probabilistically to their postsynaptic targets at the next (discrete) time step. Neuron states are updated synchronously, progressing through active, refractory, and resting phases according to well-defined transition probabilities, a key difference from the family of integrate-and-fire models [34]. Our framework captures the branching nature of spike propagation in a minimal yet biologically motivated manner. Detailed descriptions of the model components and update rules follow, along with an illustrative example.

B. Neural configuration space

The state of each neuron n at time t is described by a dynamical state variable $z_n(t) \in \mathcal{S}_n$, with values in the set $\mathcal{S}_n = \{0, 1, \dots, \tau_n\}$, where τ_n is the integer refractory period. Following activation of a neuron n from state $z_n = 0$ to state $z_n = 1$, the neuron's state evolves cyclically through the refractory states ($z_n = \{2, \dots, \tau_n\}$) starting from 2 and ending at τ_n before returning to $z_n = 0$. At time step $t = 0$, all neurons are initialized in the resting (quiescent) state, denoted by $z_n = 0$.

Therefore, at any time step t the state of the neural network can be represented by a sequence of individual neuron states

$$z(t) = (z_{e_1}(t), z_{e_2}(t), \dots, z_{e_{N_e}}(t), z_{i_1}(t), z_{i_2}(t), \dots, z_{i_{N_i}}(t)).$$

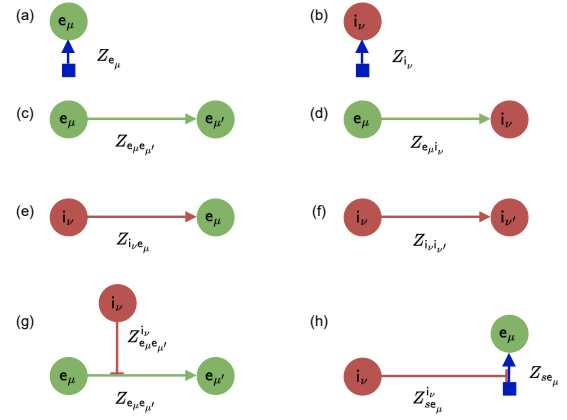


FIG. 1. Eight types of interactions defined in the GCBM. Panels illustrate: (a–b) Interactions between a neuron and an external source. (c–f) Interactions among neurons. (g) Inhibition of the excitatory-to-excitatory $E \rightarrow E$ channel. (h) Inhibition on the spontaneous activation of an excitatory neuron. Arcs are represented by arrows from the source to the target neuron. Hyperarcs are depicted as arrows with a flat line from an inhibitory neuron to another arc. Red-colored nodes and arcs denote inhibition; green nodes and arcs denote excitation. The blue box and arrow represent external spontaneous activation.

The neural network state configuration space is

$$C = \{z(t) \mid z_{e_\mu}(t) \in \mathcal{S}_e \text{ and } z_{i_\nu}(t) \in \mathcal{S}_i\}.$$

Neurons in the GCBM interact by sending and processing signals. A neuronal connection (interaction) establishes a transmission channel, labeled as nn' , meaning $(n \rightarrow n')$, represented by a directed link or arc. Those transmission channels are fixed at the start of the simulation, as we show next.

C. Types of interactions and states of arcs

The GCBM is composed of eight types of interactions shown in Fig. 1. These interactions are meant to capture biologically relevant neuronal processes, like: excitatory neurons activating other neurons, inhibitory neurons suppressing other neurons, axons from a neuron either activating or suppressing other axons, and neurons spontaneously firing. The corresponding states of the arcs at any time step t are represented as

$$Z = (Z_{e_\mu}, Z_{i_\nu}, Z_{e_\mu e_{\mu'}}, Z_{e_\mu i_\nu}, Z_{i_\nu e_\mu}, Z_{i_\nu i_{\nu'}}, Z_{e_\mu e_{\mu'}}, Z_{e_\mu}^{i_\nu}),$$

and each state is represented by a Bernoulli random variable (active [1] and inactive [0]) with a given probability of success (see Section IID). The subscripts μ, ν (and n) indicate source or target neuron. A superscript represents a hyperarc inhibition.

The first group of interactions, Fig. 1 (a–b), accounts for the experimental observation that neurons can spike

spontaneously. In the GCBM, this is modeled by external sources that deliver a spontaneous activation signal Z_n to each neuron at every timestep with probability p_{sn} . This spontaneous activation acts as a driving external input and is responsible for initiating avalanches when all neurons are in the resting state. The notation for the spontaneous activation probability, p_{sn} , is a deliberate exception: because this signal originates from an external source, the subscript is followed by e_μ or i_ν to indicate spontaneous activation of excitatory or inhibitory neurons, respectively.

The second group, Fig. 1 (c-f), accounts for the fact that chemical and electrical signals from a presynaptic neuron can alter the membrane potential of a target neuron, thereby modulating the state transition probability of a resting neuron to the active state (see Section II D). These four interactions E-E, E-I, I-E, and I-I are described by states of the arcs $Z_{e_\mu e_\mu'}$, $Z_{e_\mu i_\nu'}$, $Z_{i_\nu e_\mu'}$, and $Z_{i_\nu i_\nu'}$. The associate transmission probability are $P_{e_\mu e_\mu'}$, $P_{e_\mu i_\nu'}$, $P_{i_\nu e_\mu'}$, and $P_{i_\nu i_\nu'}$, respectively.

The third group accounts for the unique functional roles of inhibitory neurons. An inhibitory neuron can inhibit a signal on a specific dendritic branch [35]. This inhibition targets on transmission channel $Z_{e_\mu e_\mu'}$ by source inhibitory neuron i_ν , thus it is denoted by $Z_{e_\mu e_\mu'}$ with a transmission probability $P_{e_\mu e_\mu'}$. Technically, this interaction is known as a hyperarc [36]. They are visualized by a line with flat head ending on another arc in Fig. 1 (g). Another type of inhibitory interaction captures the experimental observation that inhibitory neurons can suppress spontaneous activation [37]. It is denoted by Z_{e_μ} with a transmission probability P_{e_μ} and is shown in Fig. 1 (h).

In the present study, we focus exclusively on a model where inhibitory neurons consistently inhibit as can be appreciated in Fig. 1 (f), where the arrow is red-colored. The more general case is explored in a companion paper [38].

Signal transmission across these arcs and hyperarcs occurs with a success probability that we next describe.

D. Transmission probability and network connectivity

Altogether, the transmission probabilities are represented as

$$P = (p_{se_\mu}, p_{si_\nu}, P_{e_\mu e_\mu'}, P_{e_\mu i_\nu'}, P_{i_\nu e_\mu}, P_{i_\nu i_\nu'}, P_{e_\mu e_\mu'}, P_{e_\mu}),$$

and follow a labeling pattern parallel to that of the transmission states. Each arc state is modeled as a Bernoulli random variable with success probability P , conditional on the source node being active. We refer to P as the transmission probability. The GCBM thus defines a random process on a directed hypergraph, where arcs and hyperarcs encode the complete set of neural interactions.

Network connectivity critically influences the branching dynamics observed in the model. The dynamics of the GCBM across several classes of network architectures, capable of reproducing spike rasters from laboratory experiments, were explored in a companion paper [38]. Key features of these networks served as foundational elements in the construction of the MF equations.

The first feature is the in-degree, $k_{nn'}$, defined as the number of incoming arcs to a node n' . There are four types of $k_{nn'}$ corresponding to node-to-node interaction: k_{ee} , k_{ie} , k_{ei} , and k_{ii} . While the in-degree $k_{nn'}$ may vary across interaction types in the many-body model, the MF approximation assumes a fixed $k_{nn'}$ for each interaction type. It is assumed that such a network would more closely approximate translational invariance (see Fig. 2). The second feature is the distribution of the connection weights. Experimental evidence [39, 40] suggests an exponential distribution of the in-degree weight distribution. Let $r = 1, \dots, k_{nn'}$ be the ranking order of the relative weight profile $p_r^{nn'}$, then

$$p_r^{nn'} = \frac{e^{-Br}}{\sum_{r=1}^{k_{nn'}} e^{-Br}} \quad (1)$$

where B is the bias parameter. If $B = 0$, all incoming arcs have the same weight. If $B \gg 1$, the network is essentially reduced to $k_{nn'} = 1$. The profile of the relative strength of all node-to-node arcs is assumed to have the same form. We will be using the bias parameter $B = 0.5$ throughout the paper for illustrative purposes.

The last feature of the network is the branching parameter $\kappa_{nn'}$ ($n, n' \in \{e, i\}$) that defines the transmission probabilities as: $P_{nn'}(r) = \kappa_{nn'} p_r^{nn'}$. We restrict each $\kappa_{nn'}$ to the range $[0, \kappa_{nn'}^{\max}]$, where the upper bound is given by

$$\kappa_{nn'}^{\max} = e^B \sum_{r=1}^{k_{nn'}} e^{-Br}. \quad (2)$$

If $\kappa_{nn'}$ exceeds the set maximum value, the model is no longer in a physical regime since the probability of activation of a neighborhood neuron is not restricted to the range of $[0, 1]$.

Once transmission outcomes are realized, postsynaptic neurons evaluate the resulting arc states using an activation function to determine whether they will transition to the active state, as we next illustrate.

E. Activation functions

The way a neuron processes signals is encoded in the activation function U . Define a neighborhood \mathcal{N}_n of postsynaptic neurons n as the set of the number of excitatory neurons \tilde{N}_{en} and the number of inhibitory neurons \tilde{N}_{in} inhibitory neurons that have an arc (or hyperarc) terminating at n . $\tilde{Z}_{e_\mu}(\tilde{Z}_{i_\nu})$ sequence of all arcs' states of the

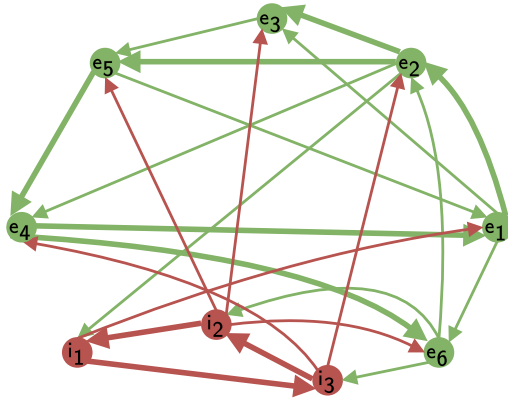


FIG. 2. Network topology of the many-body model suitable for a MF approximation. The in-degree $k_{nn'}$ is uniform across all nodes. For E-E interaction, $k_{ee} = 2$ and bias parameter $B > 0$ (incoming arcs have different weights indicated by thickness). One transmission channel is more likely to be activated than another. While $k_{ei} = k_{ie} = k_{ii} = 1$, each type has different branching parameter $\kappa_{nn'}$.

neighborhood of excitatory (inhibitory) neurons e (i),

$$\begin{aligned}\tilde{Z}_{e_{\mu'}} &= (Z_{e_{\mu'}}, Z_{e_{\mu}e_{\mu'}}, Z_{i_{\nu}e_{\mu'}}, Z_{e_{\mu}e_{\mu'}}^{i_{\nu}}, Z_{e_{\mu'}}^{i_{\nu}}) \\ \tilde{Z}_{i_{\nu'}} &= (Z_{i_{\nu'}}, Z_{e_{\mu}i_{\nu'}}, Z_{i_{\nu}i_{\nu'}}),\end{aligned}$$

where indices of the source neurons belong to $\mathcal{N}_{n'}$.

For the simplest case, where hyperarc interactions are not present, an excitatory neuron is modeled to spike when it receives more excitatory than inhibitory signals. That is, in simple informative form,

$$U(\tilde{Z}_{e'}) = \Theta \left(Z_{e'} + \sum_{e \in \mathcal{N}_{e'}} Z_{ee'} - \sum_{i \in \mathcal{N}_{e'}} Z_{ie'} \right), \quad (3)$$

where Θ is a step function with $\Theta(0) = 0$ and the summations run over all the neighborhood. Similarly, the activation function of inhibitory neuron can be $U(\tilde{Z}_{i'}) = \Theta(Z_{i'} + \sum Z_{ei'} - \sum Z_{ii'})$. However, inhibitory neurons are more diverse than excitatory neurons. Although inhibitory neighbor activity consistently decreases the likelihood of excitatory neuron firing, experimental evidence shows an opposite effect in target inhibitory neurons. Some biological mechanisms for inhibitory neurons to effectively excite other inhibitory neurons are gap junctions [41, 42], disinhibition [43], and an increase in reverse potential [43]. These modeling choices can be encoded in the activation function of an inhibitory neuron as

$$U(\tilde{Z}_{i'}) = \Theta \left(Z_{i'} + \sum_{e \in \mathcal{N}_{i'}} Z_{ei'} - \sum_{i \in \mathcal{N}_{i'}} Z_{ii'} \right). \quad (4)$$

To capture the physics of hyperarc inhibition, the ac-

tivation function must be extended to

$$\begin{aligned}U(\tilde{Z}_{e'}) = \Theta & \left(\sum_{e \in \mathcal{N}_{e'}} Z_{ee'} \cdot \prod_{i \in \mathcal{N}_{e'}} (1 - Z_{ee'}^i) - \sum_{i \in \mathcal{N}_{e'}} Z_{ie'} + \right. \\ & \left. Z_{e'} \cdot \prod_{i \in \mathcal{N}_{e'}} (1 - Z_{e'}^i) \right), \quad (5)\end{aligned}$$

where the summations and products are taken over all arcs in the neighborhood of neuron e_{μ} . If any of the hyperarcs is activated, the signal on the target arc is suppressed.

The activation function takes arc states as input and determines whether a neuron in the resting state transitions to the active state. An output of one indicates that the neuron becomes active. Since individual arc and hyperarc states are stochastic variables, the output of the activation function is also a Bernoulli random variable. In the following section, we compute the probability that the activation function gives a value of one, that is, the transition probability W_{01}^n .

F. Transition probability

To compute the transition probability of the target neuron n' , $W_{01}^{n'}$, as a function of the states $\tilde{z}_{n'}$ of its neighboring neurons,

$$\tilde{z}_{n'}(t) = (\dots, z_{e_{\mu}}, \dots; \dots, z_{i_{\nu}}, \dots), \quad e_{\mu}, i_{\nu} \in \mathcal{N}_{n'}, \quad (6)$$

one has to evaluate the expression

$$W_{01}^{n'}(\tilde{z}_{n'}(t)) = \sum_{\forall \tilde{Z}_{n'}} P(\tilde{Z}_{n'} | \tilde{z}_{n'}(t)) U(\tilde{Z}_{n'}), \quad (7)$$

which casts $W_{01}^{n'}$ in terms of the states of the neighboring neurons at a given time step t . Since $\tilde{Z}_{n'}$ are independent random variables, the conditional probabilities become

$$\begin{aligned}P(\tilde{Z}_{n'} | \tilde{z}_{n'}(t)) &= P(Z_{n'}) \cdot \prod_{\forall n \in \mathcal{N}_{n'}} P(Z_{nn'} | z_n(t)) \\ &\cdot \prod_{\forall i \in \mathcal{N}_{n'}} P(Z_{en'}^i | z_i(t)) \cdot \prod_{\forall i \in \mathcal{N}_{n'}} P(Z_{i'}^i | z_i(t)). \quad (8)\end{aligned}$$

Each of these probabilities can in turn be expressed as follows

$$\begin{aligned}P(Z_{n'}(t)) &= p_{sn'}, \\ P(Z_{nn'}(t) | z_n(t)) &= (1 - \delta_{1,z_n(t)})(1 - Z_{nn'}(t)) \\ &\quad + \delta_{1,z_n(t)} ((1 - Z_{nn'}(t))(1 - P_{nn'}) + Z_{nn'}(t)P_{nn'}), \\ P(Z_{ee'}^i(t) | z_i(t)) &= (1 - \delta_{1,z_i(t)})(1 - Z_{ee'}^i(t)) \\ &\quad + \delta_{1,z_i(t)} ((1 - Z_{ee'}^i(t))(1 - P_{ee'}^i) + Z_{ee'}^i(t)P_{ee'}^i), \\ P(Z_{e'}^i(t) | z_i(t)) &= (1 - \delta_{1,z_i(t)})(1 - Z_{e'}^i(t)) \\ &\quad + \delta_{1,z_i(t)} ((1 - Z_{e'}^i(t))(1 - P_{e'}^i) + Z_{e'}^i(t)P_{e'}^i). \quad (9)\end{aligned}$$

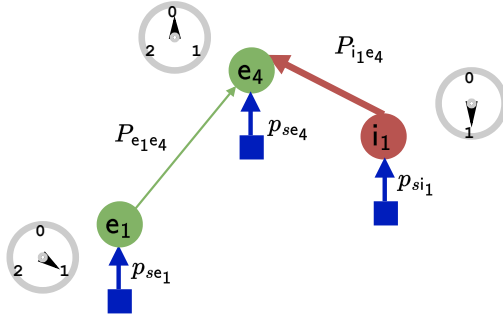


FIG. 3. Neighborhood of excitatory neuron e_4 . Green nodes represent excitatory neurons and red nodes represent inhibitory neurons. Directed arrows indicate synaptic interactions: green for excitation and red for inhibition. The layout includes all neurons and interactions directly linked to e_4 , capturing its environment. The clocks in each of the nodes represent its state z_n . The arcs are labeled by the probability of activation.

For the MF analysis in Section III, we find that computationally the only transition probability that must be evaluated explicitly is the special case in which all neighboring neurons are active, i.e., $\tilde{z}_n(t) = (1, \dots; 1, \dots)$, which is labeled as \overline{W}_{01}^n . To proceed, we construct the corresponding event space necessary for computing \overline{W}_{01}^n .

We first define the event $Z_{n'}(t) = 1(0)$ to indicate that the directed edge from the spontaneous source to neuron n' is active (inactive) at time t . Next, consider the set of directed edge states $Z_{nn'}(t)$. We define $Z_{nn'}(t) = 1(0)$ to indicate that the directed edge from neuron n to neuron n' is active (inactive). Similarly, the events $Z_{ee'}^i(t) = 1(0)$ and $Z_{e'e}^i(t) = 1(0)$ denote that the corresponding hyperarc originating from inhibitory neuron i is active (inactive).

Since excitatory signals can be canceled by arc-to-arc inhibition as specified by the activation function, we define the complete set of events that actually contribute to the activation of neuron n at time t as follows

$$\begin{aligned} A_0^e(t) &= (Z_e(t) = 1) \bigcap_{i_\nu \in \mathcal{N}_e} (Z_{e_\nu}^i(t) = 0), \\ A_0^i(t) &= (Z_i(t) = 1), \\ A_\mu^e(t) &= (Z_{e_\mu e}(t) = 1) \bigcap_{i_\nu \in \mathcal{N}_e} (Z_{e_\mu e}^i(t) = 0), \\ A_\mu^i(t) &= (Z_{e_\mu i}(t) = 1), \\ B_\nu^n(t) &= (Z_{i_\nu n}(t) = 1), \end{aligned} \quad (10)$$

where $\mu \in \{1, \dots, \tilde{N}_{\text{en}}\}$ ($\nu \in \{1, \dots, \tilde{N}_{\text{in}}\}$) indexes the excitatory (inhibitory) neighbors of n .

The probabilities of the events $A_0^n(t)$, $A_\mu^n(t)$ and $B_\nu^n(t)$ conditioned on all (source) neighboring neurons being in

the active state, are given by

$$\begin{aligned} P(A_0^e(t) | \tilde{z}_n = (1, \dots; 1, \dots)) &= p_{se} \prod_{i_\nu \in \mathcal{N}_e} (1 - P_{e_\nu}^{i_\nu}), \\ P(A_0^i(t) | \tilde{z}_n = (1, \dots; 1, \dots)) &= p_{si}, \\ P(A_\mu^e(t) | \tilde{z}_n = (1, \dots; 1, \dots)) &= P_{e_\mu e} \prod_{i_\nu \in \mathcal{N}_e} (1 - P_{e_\mu e}^{i_\nu}), \\ P(A_\mu^i(t) | \tilde{z}_n = (1, \dots; 1, \dots)) &= P_{e_\mu i}, \\ P(B_\nu^n(t) | \tilde{z}_n = (1, \dots; 1, \dots)) &= P_{i_\nu n}, \end{aligned} \quad (11)$$

which we will next compactly denote as $\overline{P}(A_0^n)$, $\overline{P}(A_\mu^n)$, and $\overline{P}(B_\nu^n)$.

With the events $A_0^n(t)$, $A_\mu^n(t)$ and $B_\nu^n(t)$ and their corresponding conditional probabilities defined, we next introduce E_m^n as the probability that at least m of the events $A_0^n(t), \dots, A_{\tilde{N}_{\text{en}}}^n(t)$ occur simultaneously. The probability E_m^n can be computed using a generalization of the inclusion-exclusion principle

$$E_m^n = \sum_{r=m}^{\tilde{N}_{\text{en}}+1} (-1)^{r-m} \binom{r-1}{m-1} S_r^{\text{en}}, \quad m = 1, \dots, \tilde{N}_{\text{en}} + 1, \quad (12)$$

where

$$S_r^{\text{en}} := \sum_{\ell_r=1}^{L_r} \overline{P} \left(\bigcap_{j \in J_{\ell_r}} A_j^n \right), \quad (13)$$

with $J_{\ell_r} \subseteq \{0, \dots, \tilde{N}_{\text{en}}\}$ denoting a subset of cardinality r . The index ℓ_r runs over all such subsets, of which there are $L_r = \binom{\tilde{N}_{\text{en}}+1}{r}$. The events A_0^n and A_μ^n are assumed to be independent.

Similarly, we define $I_{[m]}^n$ as the probability that exactly m of the events $B_1^n(t), \dots, B_{\tilde{N}_{\text{in}}}^n(t)$ simultaneously occur,

$$I_{[m]}^n = \sum_{r=m}^{\tilde{N}_{\text{in}}} (-1)^{r-m} \binom{r}{m} S_r^{\text{in}}, \quad m = 0, \dots, \tilde{N}_{\text{in}}, \quad (14)$$

where

$$S_r^{\text{in}} := \sum_{\ell_r=1}^{M_r} \overline{P} \left(\bigcap_{j \in K_{\ell_r}} B_j^n \right), \quad (15)$$

with $K_{\ell_r} \subseteq \{1, \dots, \tilde{N}_{\text{in}}\}$ denoting a subset of cardinality r . The index ℓ_r runs over all such subsets, of which there are $M_r = \binom{\tilde{N}_{\text{in}}}{r}$. Note that $S_0^{\text{in}} = 1$. The events B_ν^n are also assumed to be independent. The probability of at least m of the events occurring simultaneously, or the probability of exactly m of the events occurring simultaneously, is calculated from a generalization of the inclusion-exclusion principle known as the Schuette-Nesbitt formula [44].

z_{e_1}	z_{i_1}	$W_{01}^{e_4}$
✓	✗	p_{se_4}
✗	1	$p_{se_4}(1 - P_{i_1 e_4})$
1	✗	$p_{se_4} + P_{e_1 e_4} - p_{se_4} P_{e_1 e_4}$
1	1	$(p_{se_4} + P_{e_1 e_4} - p_{se_4} P_{e_1 e_4})(1 - P_{i_1 e_4}) + p_{se_4} P_{e_1 e_4} P_{i_1 e_4}$

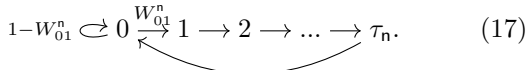
TABLE I. Transition probabilities, $W_{01}^{e_4}$, of a node transitioning from state 0 to state 1 under various neighbor conditions. The transition probability increases when an excitatory neighbor is active and decreases when an inhibitory neighbor is active. The symbol \checkmark represents a node that is not active, i.e., $0, 2, \dots, \tau_n$, and τ_n denotes the time constant for the node's state evolution. There is always a chance of spontaneous activation even when the neighbors' states are not active.

To compute $\overline{W_{01}^n}$, we consider the activation function U in Eq. (7), which includes only terms for which the number of active excitatory arcs (excluding those subject to arc-to-arc inhibition) exceeds the number of active inhibitory arcs by at least one, thereby contributing to activation of the target neuron. By accounting for the possible number of \tilde{N}_{en} and \tilde{N}_{in} , the general expression of $\overline{W_{01}^n}$ is

$$\overline{W_{01}^n} = W_{01}^n((1, \dots, 1, \dots)) = \sum_{m=1}^{\tilde{N}_{in}+1} E_m^n I_{[m-1]}^n. \quad (16)$$

G. Neuronal Dynamics

Having established the components necessary to define the stochastic dynamics of the GCBM, we now proceed with a systematic description. Each neuron has its own probability W_{01}^n of transitioning from the quiescent state (0) at time t to the active state (1) at time $t+1$. Only neurons in the quiescent state integrate inputs and may spike with probability W_{01}^n . This process is illustrated in the following diagram:



The only stochastic component in the dynamics is the transition probability W_{01}^n , through which neurons may be activated by incoming signals. Once activated, a neuron enters a dormant phase lasting τ_n time steps, representing the biological refractory period. Neurons in the active or refractory states evolve deterministically in a fixed cycle and do not process incoming inputs during this time.

In summary, the neuronal dynamics of the GCBM is described by the following algorithm:

1. *Initialization:* All neuronal interactions are defined by a fixed hypergraph—whose topology plays a critical role [38]—as described in Section II C. The initial state of each neuron is set to $z_n(t=0) = 0$.

2. *Drive:* At each time step t , every neuron n' receives a spontaneous signal with probability $p_{sn'}$ (Section II D).

3. *Relaxation:* If a presynaptic neuron n is in the active state, $z_n(t) = 1$, it transmits a set of signals Z through all its outgoing channels with transmission probability P , as described in Section II D.

- If the postsynaptic neuron n' is in the quiescent state, $z_{n'}(t) = 0$, it may transition to the active state, $z_{n'}(t+1) = 1$, by processing incoming signals and evaluating the activation function U , as described in Section II E. With P and U evaluated for each target neuron n' , we then compute the transition probability $W_{01}^{n'}$, as detailed in Section II F.
- If the postsynaptic neuron n' is in a state $z_{n'}(t) \neq 0$, it progresses to the next refractory state until it returns to the quiescent state. This evolution is governed by

$$z_{n'}(t+1) = (z_{n'}(t) + 1) \bmod (\tau_{n'} + 1),$$

as illustrated in the diagram (17).

4. *Iteration:* Start the next time step: Return to step 2.

H. Dynamics Characterization

The density of active excitatory nodes has previously been identified as the order parameter of the CBM [13]. For the GCBM, we introduce the density of active excitatory and inhibitory nodes:

$$\rho_1^e(t) = \frac{1}{N_e} \sum_{\mu=1}^{N_e} \delta_{z_{e_\mu}(t), 1}, \quad \rho_1^i(t) = \frac{1}{N_i} \sum_{\nu=1}^{N_i} \delta_{z_{i_\nu}(t), 1}. \quad (18)$$

The time average case is

$$\bar{\rho}_1^n = \langle \rho_1^n(t) \rangle_t = \frac{1}{N_T} \sum_{t=1}^{N_T} \rho_1^n(t), \quad (19)$$

where N_T is the number of iteration time steps of the map. The zero-field dynamical susceptibility χ_n corresponds to the fluctuations

$$\chi_n = N_n \left(\langle \rho_1^n(t) \rangle_t^2 - \langle \bar{\rho}_1^n \rangle^2 \right) \quad (20)$$

and quantifies the dynamical response of the system.

III. HIERARCHY OF MEAN-FIELD APPROXIMATIONS

Now that we have established the many-body formulation of the GCBM, we aim to develop a semi-analytical

method to probe its dynamics. The GCBM has been shown to reproduce avalanche behavior consistent with experimental observations [17, 38, 40]. As noted earlier, the GCBM falls within the NP class of problems, meaning that many-body simulations of the GCBM would require exponentially more computations as more nodes are added, limiting the potential for numerical examination and insights. The goal of the MF approximation is to derive expressions for the fraction of neurons in a given state j at time step t , within a framework that generalizes across a range of network topologies. This framework relies on a series of assumptions that simplify the underlying network dynamics.

First, we enforce translational invariance to reduce the complex interactions in a network of N neurons to a tractable system involving a single representative excitatory neuron, e_0 , and a single representative inhibitory neuron, i_0 . In general, a motif may contain multiple representative neurons of each type. For pedagogical clarity, however, we restrict our examples to a single representative neuron of each type. This choice of using only a single representative neuron ensures that the number of neighbors coincides with the in-degree, so that $\tilde{N}_{nn'} = k_{nn'}$. The state of the representative neurons is $z_{n_0}(t)$. The neighborhoods of these representative neurons are characterized by the distribution of neuron states and the connectivity structure of the many-body network. By varying the form of these effective interactions, the model can represent the collective behavior across a hierarchy of network topologies. Second, we assume that the dynamical states of neighboring neurons, denoted $\tilde{z}_{n_0}(t)$, are statistically independent and identically distributed (i.i.d.). Finally, we assume the probability of finding the representative neuron n_0 in state j corresponds to the density of neurons in state j in the full many-body system.

Under these assumptions, the MF approximation replaces the many-body network with a *motif* whose dynamics are governed by coupled nonlinear maps. This approach offers a tractable semi-analytical framework for studying network stability, the influence of inhibitory neurons, the model's consistency with the quasi-critical hypothesis, and the onset of chaotic dynamics.

A. Motifs and representative neurons

An example of a spatially symmetric network composed of $N_e + N_i$ neurons, to which the MF approximation can be applied, is shown in Fig. 4 (a). This panel consists of excitatory and inhibitory neurons with their interactions. Figure 4 (b) illustrates representative subgraphs that capture the interactions experienced by a neuron in this network. The MF approximation reduces the full network to two representative neurons, one excitatory neuron, e_0 , and one inhibitory neuron, i_0 , each interacting with a set of MF neighbors. Specifically, e_0 receives input from one spontaneous source and one excitatory neighbor, and one inhibitory neighbor. In contrast, i_0 receives input from one spontaneous source and one excitatory neighbor. These neighbors are denoted by \bar{n} to indicate that they represent the average effective environment rather than specific neurons. The dynamics are defined solely on the representative neurons e_0 and i_0 . These two subgraphs are then merged into a single motif, shown in Fig. 5, where both e_0 and i_0 share the same environment.

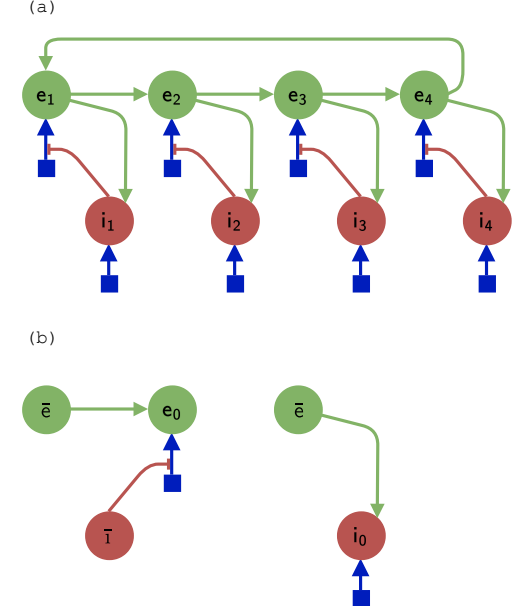


FIG. 4. An example network and its subgraphs in the GCBM. (a): A translationally invariant network where every neuron has the same local presynaptic environment. Each excitatory neuron receives one incoming excitatory arc, one inhibitory arc, and one external spontaneous activation arc. Each inhibitory neuron receives one excitatory arc and one external spontaneous activation arc. (b): The subgraphs used in the MF approximation. We have $\tilde{N}_{e_0} = \tilde{N}_{e_{i_0}} = \tilde{N}_{i_{e_0}} = 1$, and $\tilde{N}_{i_{i_0}} = 0$. Here, e_0 denotes the representative excitatory neuron and i_0 the representative inhibitory neuron, while \bar{e} and \bar{i} represent the mean excitatory and inhibitory neighbors, respectively. Blue arrows denote external spontaneous activation.

tory neighbor, and one inhibitory neighbor. In contrast, i_0 receives input from one spontaneous source and one excitatory neighbor. These neighbors are denoted by \bar{n} to indicate that they represent the average effective environment rather than specific neurons. The dynamics are defined solely on the representative neurons e_0 and i_0 . These two subgraphs are then merged into a single motif, shown in Fig. 5, where both e_0 and i_0 share the same environment.

B. Dynamical maps

The MF approximation expresses excitatory and inhibitory neuron state densities at time $t+1$ as functions of those at time t . The only nontrivial state densities are the probability of activation of excitatory and inhibitory neurons, respectively, due to their stochastic dynamics.

To derive the dynamical maps of these nontrivial terms, consider a representative neuron n_0 and its mean neighborhood. Let the *joint probability* of neuron's state $z_{n_0}(t)$ at time t and $t+1$, along with the state of its neighborhood \tilde{z}_{n_0} , be denoted by $P(z_{n_0}(t+1), z_{n_0}(t), \tilde{z}_{n_0}(t))$.

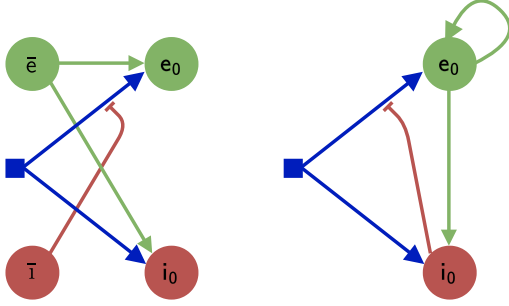


FIG. 5. Example motif of the network in Fig. 4. This is an example of how we form the motif from the network subgraphs. This example includes the inhibition of a directed edge of the external spontaneous activation. The motif has all the mean neighborhood connections on the left and the representative neurons on the right, showing the progression of time from left to right. A MF diagram is also shown on the right to emphasize that there are only two representative neurons in the MF approximation. We will primarily use the *unfold* diagram on the left to clearly show the neighborhood. We have $\tilde{N}_{e_0} = \tilde{N}_{i_0} = \tilde{N}_{\bar{e}_0} = 1$, and $\tilde{N}_{\bar{i}_0} = 0$. Here, e_0 denotes the representative excitatory neuron and i_0 the representative inhibitory neuron, while \bar{e} and \bar{i} represent the mean excitatory and inhibitory neighbors, respectively. Blue arrows denote external spontaneous activation.

We are interested in $P(z_{n_0}(t+1) = 1)$. Therefore, from the law of total probability

$$\begin{aligned} P(z_{n_0}(t+1) = 1) \\ = \sum_{\forall \tilde{z}_{n_0}(t)} \sum_{j=0}^{\tau_n} P(z_{n_0}(t+1) = 1, z_{n_0}(t) = j, \tilde{z}_{n_0}(t)), \end{aligned} \quad (21)$$

where summation runs over all possible states of the neighborhood. From the GCBM transition rules, only $z_{n_0}(t) = 0$ can transit to $z_{n_0}(t+1) = 1$. Thus

$$\begin{aligned} P(z_{n_0}(t+1) = 1) \\ = \sum_{\forall \tilde{z}_{n_0}(t)} P(z_{n_0}(t+1) = 1, z_{n_0}(t) = 0, \tilde{z}_{n_0}(t)). \end{aligned} \quad (22)$$

This can be evaluated using the conditional probability

$$\begin{aligned} P(z_{n_0}(t+1) = 1) \\ = \sum_{\forall \tilde{z}_{n_0}(t)} W_{01}^{n_0}(\tilde{z}_{n_0}(t)) \cdot P(z_{n_0}(t) = 0, \tilde{z}_{n_0}(t)), \end{aligned} \quad (23)$$

where $W_{01}^{n_0}(\tilde{z}_{n_0}(t)) = P(z_{n_0}(t+1) = 1 | z_{n_0}(t) = 0, \tilde{z}_{n_0}(t))$.

In the many-body problem, the joint probability $P(z_{n_0}(t) = 0, \tilde{z}_{n_0}(t))$ can be very complex. Using our second primary assumption that neuron states are *independent random variables*, we approximate this joint probability as the product of individual probabilities

$$\begin{aligned} P(z_{n_0}(t) = 0, \tilde{z}_{n_0}(t)) \\ = P(z_{n_0}(t) = 0) \cdot \prod_{\mu=1}^{\tilde{N}_{e_0}} P(\tilde{z}_{e_\mu}(t)) \cdot \prod_{\nu=1}^{\tilde{N}_{i_0}} P(\tilde{z}_{i_\nu}(t)). \end{aligned} \quad (24)$$

Moreover, it is assumed that the state of all excitatory and inhibitory neurons is drawn from an *identical probability mass distribution*. That is

$$P(z_n(t) = m) = P(z_{n'}(t) = m), \quad \forall m \in \mathcal{S}_n. \quad (25)$$

To simplify notation, let $x_m(t)$ denote the probability that an excitatory neuron e_μ is in state m at time step t . (The neuron index is omitted due to the assumption of an identical mass distribution across excitatory neurons.) Similarly, let $y_n(t)$ represent the probability that an inhibitory neuron i_ν is in state n at time step t

$$\begin{aligned} x_m(t) &\triangleq P(z_{e_\mu}(t) = m) \quad m \in \mathcal{S}_e, \\ y_n(t) &\triangleq P(z_{i_\nu}(t) = n) \quad n \in \mathcal{S}_i. \end{aligned} \quad (26)$$

In other words, we impose that the representative neurons and their neighbors are statistically indistinguishable, sharing the same state distribution. This is the MF approximation, leading to a set of dynamical *self-consistent equations* that we show next.

The MF equations for $m = 1$ are given by the dynamical maps for e_0 and i_0 as follows

$$x_1(t+1) = F \cdot x_0(t), \quad (27)$$

$$F = \sum_{\forall \tilde{z}_{e_0}(t)} W_{01}^{e_0}(\tilde{z}_{e_0}(t)) \cdot \prod_{\mu=1}^{\tilde{N}_{e_0}} x_{z_{e_\mu}}(t) \cdot \prod_{\nu=1}^{\tilde{N}_{i_0}} y_{z_{i_\nu}}(t), \quad (28)$$

$$y_1(t+1) = G \cdot y_0(t), \quad (29)$$

$$G = \sum_{\forall \tilde{z}_{i_0}(t)} W_{01}^{i_0}(\tilde{z}_{i_0}(t)) \cdot \prod_{\mu=1}^{\tilde{N}_{e_0}} x_{z_{e_\mu}}(t) \cdot \prod_{\nu=1}^{\tilde{N}_{i_0}} y_{z_{i_\nu}}(t), \quad (30)$$

where $x_1(t)$ ($y_1(t)$) represents the MF approximation to $\rho_1^e(t)$ ($\rho_1^i(t)$). These maps relate the probability that the representative neuron is active at time $t+1$ to its own state and the states of its neighbors at time t .

To complete the set of MF equations, the refractory periods must be taken into account. Once a neuron enters a refractory state, it progresses deterministically—advancing one step at a time—until it reaches the final refractory state. It then transitions to the quiescent state (0) in the subsequent time step

$$\begin{aligned} x_m(t+1) &= x_{m-1}(t), \quad 2 \leq m \leq \tau_e, \quad t \geq 1 \\ y_n(t+1) &= y_{n-1}(t), \quad 2 \leq n \leq \tau_i, \quad t \geq 1 \end{aligned} \quad (31)$$

Thus, there are $\tau_e + \tau_i$ dynamical variables, each subject to specific constraints. Since $x_m(t)$ and $y_n(t)$ represent probabilities for each m and n , they are confined to the interval $[0, 1]$ and must satisfy normalization conditions

$$\begin{aligned} 0 \leq x_m(t) \leq 1, \quad \forall t \quad \text{and} \quad \forall m \in \mathcal{S}_e, \\ 0 \leq y_n(t) \leq 1, \quad \forall t \quad \text{and} \quad \forall n \in \mathcal{S}_i, \\ \sum_{m=0}^{\tau_e} x_m(t) = 1, \quad \forall t, \quad \sum_{n=0}^{\tau_i} y_n(t) = 1, \quad \forall t \end{aligned} \quad (32)$$

With these restrictions we can define $x_0(t)$ and $y_0(t)$ as

$$x_0(t) = 1 - \sum_{m=1}^{\tau_e} x_m(t), \quad y_0(t) = 1 - \sum_{n=1}^{\tau_i} y_n(t). \quad (33)$$

Consequently, Eqs. (27), (29), and (31), together with the constraints in (32), form a set of coupled nonlinear dynamical maps that define the GCBM MF approximation. What remains is the computation of the transition probabilities $W_{01}^{n_0}(\tilde{z}_{n_0}(t))$. These depend on the specific motif under consideration, as will be demonstrated in the following section.

C. Dictionary of Mean-Field Approximations

In general, computing the MF equations requires evaluating the transition probabilities for all possible configurations of neighboring neurons. However, in this section, we will show that this is not necessary. Instead, it is sufficient to compute the transition probability for the case where all neighboring neurons are active, that is $W_{01}^{n_0}$ in Eq. (16). (Note we use n_0 since we are referring to MF approximations.) Then, to get from this transition probability to the MF equations it is necessary to apply a substitution rule, such that the transmission probabilities are multiplied by the probability that the corresponding neighboring neuron is active. This procedure establishes a direct dictionary between any network motif and its corresponding MF equations.

More explicitly, to derive the MF equations, Eqs. (27) and (29), we begin by evaluating the term $\overline{W}_{01}^{n_0}$ in Eq. (16), which provides a compact starting expression. The next step is to substitute the variables defined in Eqs. (12), (13), (14), and (15), followed by explicitly specifying the probabilities of the relevant events from Eqs. (11). This procedure yields the transition probability for the configuration in which all neighboring neurons are active, expressed in terms of the transmission probabilities. Although these are written with general indices, in the MF approximation we restrict to e_0 and i_0 . The final step is to apply the following substitution rules to $\overline{W}_{01}^{e_0}$ and $\overline{W}_{01}^{i_0}$ to obtain F and G , respectively,

$$\begin{aligned} \overline{W}_{01}^{e_0}(p_{se_0}, P_{e_\mu e_0}, P_{i_\nu e_0}, P_{e_\mu e_0}^{i_\nu}, P_{e_0}^{i_\nu}, \dots) &\rightarrow F = \\ \overline{W}_{01}^{e_0}(p_{se_0}, P_{e_\mu e_0} x_1(t), P_{i_\nu e_0} y_1(t), P_{e_\mu e_0}^{i_\nu} y_1(t), P_{e_0}^{i_\nu} y_1(t), \dots) \\ \overline{W}_{01}^{i_0}(p_{si_0}, P_{e_\mu i_0}, P_{i_\nu i_0}, \dots) &\rightarrow G = \\ \overline{W}_{01}^{i_0}(p_{si_0}, P_{e_\mu i_0} x_1(t), P_{i_\nu i_0} y_1(t), \dots), \quad \forall e_\mu, i_\nu. \end{aligned} \quad (34)$$

To demonstrate the validity of these substitution rules, we first consider a simplified setting in which arc-arc interactions are neglected. The general case, including all arc-arc interaction terms, is presented in Appendix B.

Starting from the MF equations, and substituting the transition probabilities $W_{01}^{e_0}(\tilde{z}_{e_0}(t))$ and $W_{01}^{i_0}(\tilde{z}_{i_0}(t))$ using

Eq. (7), it can be shown that F and G can be expressed as

$$F = \sum_{\forall \tilde{Z}_{e_0}} U(\tilde{Z}_{e_0}) \cdot p_{se_0} \cdot \sum_{z_{e_1}(t)=0}^{\tau_e} P(Z_{e_1 e_0} | z_{e_1}(t)) \cdot x_{z_{e_1}(t)} \cdots, \quad (35)$$

$$G = \sum_{\forall \tilde{Z}_{i_0}} U(\tilde{Z}_{i_0}) \cdot p_{si_0} \cdot \sum_{z_{e_1}(t)=0}^{\tau_e} P(Z_{e_1 i_0} | z_{e_1}(t)) \cdot x_{z_{e_1}(t)} \cdots. \quad (36)$$

After some algebraic manipulations, and using the arc activation functions in Eq. (9), the functions F and G can be written as

$$\begin{aligned} F = \sum_{\forall \tilde{Z}_{e_0}} U(\tilde{Z}_{e_0}) \cdot p_{se_0} \cdot \prod_{\mu=1}^{\tilde{N}_{ee_0}} ((1 - P_{e_\mu e_0} x_1(t)) \delta_{0, Z_{e_\mu e_0}} + \\ P_{e_\mu e_0} x_1(t) \delta_{1, Z_{e_\mu e_0}}) \cdot \prod_{\nu=1}^{\tilde{N}_{ie_0}} ((1 - P_{i_\nu e_0} y_1(t)) \delta_{0, Z_{i_\nu e_0}} + \\ P_{i_\nu e_0} y_1(t) \delta_{1, Z_{i_\nu e_0}}), \end{aligned} \quad (37)$$

$$\begin{aligned} G = \sum_{\forall \tilde{Z}_{i_0}} U(\tilde{Z}_{i_0}) \cdot p_{si_0} \cdot \prod_{\mu=1}^{\tilde{N}_{ie_0}} ((1 - P_{e_\mu i_0} x_1(t)) \delta_{0, Z_{e_\mu i_0}} + \\ P_{e_\mu i_0} x_1(t) \delta_{1, Z_{e_\mu i_0}}) \cdot \prod_{\nu=1}^{\tilde{N}_{ii_0}} ((1 - P_{i_\nu i_0} y_1(t)) \delta_{0, Z_{i_\nu i_0}} + \\ P_{i_\nu i_0} y_1(t) \delta_{1, Z_{i_\nu i_0}}). \end{aligned} \quad (38)$$

Starting with Eq. (7) one can write the cases when all the neighbors are active $\overline{W}_{01}^{e_0}$ and $\overline{W}_{01}^{i_0}$ as

$$\begin{aligned} \overline{W}_{01}^{e_0} = \sum_{\forall \tilde{Z}_{e_0}} U(\tilde{Z}_{e_0}) \cdot p_{se_0} \cdot \prod_{\mu=1}^{\tilde{N}_{ee_0}} ((1 - P_{e_\mu e_0}) \delta_{0, Z_{e_\mu e_0}} + \\ P_{e_\mu e_0} \delta_{1, Z_{e_\mu e_0}}) \cdot \prod_{\nu=1}^{\tilde{N}_{ie_0}} ((1 - P_{i_\nu e_0}) \delta_{0, Z_{i_\nu e_0}} + \\ P_{i_\nu e_0} \delta_{1, Z_{i_\nu e_0}}), \end{aligned} \quad (39)$$

$$\begin{aligned} \overline{W}_{01}^{i_0} = \sum_{\forall \tilde{Z}_{i_0}} U(\tilde{Z}_{i_0}) \cdot p_{si_0} \cdot \prod_{\mu=1}^{\tilde{N}_{ie_0}} ((1 - P_{e_\mu i_0}) \delta_{0, Z_{e_\mu i_0}} + \\ P_{e_\mu i_0} \delta_{1, Z_{e_\mu i_0}}) \cdot \prod_{\nu=1}^{\tilde{N}_{ii_0}} ((1 - P_{i_\nu i_0}) \delta_{0, Z_{i_\nu i_0}} + \\ P_{i_\nu i_0} \delta_{1, Z_{i_\nu i_0}}), \end{aligned} \quad (40)$$

expressions that differ from F and G by the fact that, in the latter, each transmission probability is multiplied by the probability that the corresponding neighboring neuron is active. This means that Eq. (16) together with the substitution rules in Eq. (34) provides a complete dictionary for constructing the MF equations associated with each network motif. An explicit example illustrating this methodology is presented in the following section.

IV. EXAMPLE MOTIFS WITH PROBABILITY OF ACTIVATION COMPUTATION

For pedagogical reasons, we start with the simple motif shown in Fig. 6 which has $\tilde{N}_{\text{ee}_0} = \tilde{N}_{\text{ie}_0} = 1$, and $\tilde{N}_{\text{ei}_0} = \tilde{N}_{\text{ii}_0} = 0$. For this example, we set $\tau_e = \tau_i = 2$, which yields $(1+1)^2 = 4$ possible configurations for the motif. For this example, e_1 and i_1 represent \bar{e} and \bar{i} the mean neighborhood shown in Fig. 5.

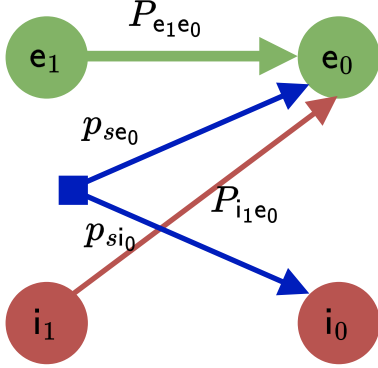


FIG. 6. This motif has site inhibition with a number of excitatory neighboring neurons $\tilde{N}_{\text{ee}_0} = 1$, a number of inhibitory neighboring neurons $\tilde{N}_{\text{ie}_0} = 1$, and no neighbors for the target inhibitory neuron z_{i_0} . In this figure, e_1 and i_1 represent \bar{e} and \bar{i} the mean neighborhood shown in Fig. 5.

The first transition probability function, $W_{01}^{\text{no}}(\tilde{z}_{n_0}(t))$, we will compute corresponds to the case where $\tilde{z}_{e_1} = 1$, $\tilde{z}_{i_1} = 1$; in other words, it is $\overline{W_{01}^{\text{no}}} = W_{01}^{\text{no}}((1;1))$. Here, we assume $p_{se_\mu} = p_{si_\nu} = p_s$. We start computing the transition probability $\overline{W_{01}^{\text{e}_0}}$ using Eq. (16)

$$\begin{aligned} \overline{W_{01}^{\text{e}_0}} &= E_1^{\text{e}_0} I_{[0]}^{\text{e}_0} + E_2^{\text{e}_0} I_{[1]}^{\text{e}_0} \quad (41) \\ &= (p_s + (1-p_s)P_{e_1e_0})(1 - P_{i_1e_0}) + p_s P_{e_1e_0} P_{i_1e_0}. \end{aligned}$$

Similarly,

$$\overline{W_{01}^{\text{i}_0}} = E_1^{\text{i}_0} I_{[0]}^{\text{i}_0} = p_s. \quad (42)$$

In Appendix C, we provide detailed steps showing how to compute $\overline{W_{01}^{\text{e}_0}}$ and $\overline{W_{01}^{\text{i}_0}}$.

Next, we compute F and G by applying the substitution rule, Eqs. (34), to $\overline{W_{01}^{\text{no}}}$. The resulting dynamical

map $x_{1,2}(t), y_{1,2}(t)$ becomes

$$\begin{aligned} x_1(t+1) &= x_0(t)((p_s + (1-p_s)P_{e_1e_0}x_1(t))(1 - P_{i_1e_0}y_1(t)) \\ &\quad + p_s P_{e_1e_0}x_1(t)P_{i_1e_0}y_1(t)) \\ x_2(t+1) &= x_1(t) \\ y_1(t+1) &= y_0(t) p_s \\ y_2(t+1) &= y_1(t). \end{aligned} \quad (43)$$

The validity of the substitution rule for this example is demonstrated explicitly in Appendix D, where we show how to compute *all* transition probabilities $W_{01}^{\text{no}}(\tilde{z}_{n_0}(t))$.

Now that we have established how the transition probabilities and maps are established, we turn to the more representative motif shown in Fig. 7, which will be used in subsequent sections to describe the solutions of the GCBM MF equations. We will apply the same procedure to compute the maps in Eqs. (27) and (29) for this motif. The representative motif is chosen such that $\tilde{N}_{\text{ee}_0} = \tilde{N}_{\text{ie}_0} = \tilde{N}_{\text{ei}_0} = \tilde{N}_{\text{ii}_0} = 2$. We refrain from assigning fixed values to τ_e and τ_i , as these parameters will be varied in subsequent examples. For this example, (e_1, e_2) and (i_1, i_2) represent \bar{e} and \bar{i} , the mean neighborhoods shown in Fig. 5. Starting with computing the transition probability when all neighbors are active $\overline{W_{01}^{\text{no}}} = W_{01}^{\text{no}}((1, 1; 1, 1))$

$$\begin{aligned} \overline{W_{01}^{\text{e}_0}} &= E_1^{\text{e}_0} I_{[0]}^{\text{e}_0} + E_2^{\text{e}_0} I_{[1]}^{\text{e}_0} + E_3^{\text{e}_0} I_{[2]}^{\text{e}_0} \quad (44) \\ &= (p_s + (1-p_s)(P_{e_1e_0} + P_{e_2e_0} - P_{e_1e_0}P_{e_2e_0})) \\ &\quad ((1 - P_{i_1e_0})(1 - P_{i_2e_0})) + \\ &\quad (p_s(P_{e_1e_0} + P_{e_2e_0}) + (1 - 2p_s)P_{e_1e_0}P_{e_2e_0}) \\ &\quad (P_{i_1e_0} + P_{i_2e_0} - 2P_{i_1e_0}P_{i_2e_0}) + p_s P_{e_1e_0}P_{e_2e_0}P_{i_1e_0}P_{i_2e_0}. \end{aligned}$$

$$\begin{aligned} \overline{W_{01}^{\text{i}_0}} &= E_1^{\text{i}_0} I_{[0]}^{\text{i}_0} + E_2^{\text{i}_0} I_{[1]}^{\text{i}_0} + E_3^{\text{i}_0} I_{[2]}^{\text{i}_0} \quad (45) \\ &= (p_s + (1-p_s)(P_{e_1i_0} + P_{e_2i_0} - P_{e_1i_0}P_{e_2i_0})) \\ &\quad ((1 - P_{i_1i_0})(1 - P_{i_2i_0})) + \\ &\quad (p_s(P_{e_1i_0} + P_{e_2i_0}) + (1 - 2p_s)P_{e_1i_0}P_{e_2i_0}) \\ &\quad (P_{i_1i_0} + P_{i_2i_0} - 2P_{i_1i_0}P_{i_2i_0}) + p_s P_{e_1i_0}P_{e_2i_0}P_{i_1i_0}P_{i_2i_0}. \end{aligned}$$

The steps for computing $\overline{W_{01}^{\text{no}}}$ are omitted due to the extensive length. Applying the substitution rule, Eq. (34), to the equation above leads to the dynamical map expressed as polynomial sums

$$\begin{aligned} x_1(t+1) &= x_0(t) \sum_{c=0, d=0}^2 a_{cd} x_1(t)^c y_1(t)^d, \\ x_m(t+1) &= x_{m-1}(t), \quad \text{for } 2 \leq m \leq \tau_e \end{aligned} \quad (46)$$

and

$$\begin{aligned} y_1(t+1) &= y_0(t) \sum_{c=0, d=0}^2 b_{cd} x_1(t)^c y_1(t)^d, \\ y_n(t+1) &= y_{n-1}(t), \quad \text{for } 2 \leq n \leq \tau_i \end{aligned} \quad (47)$$

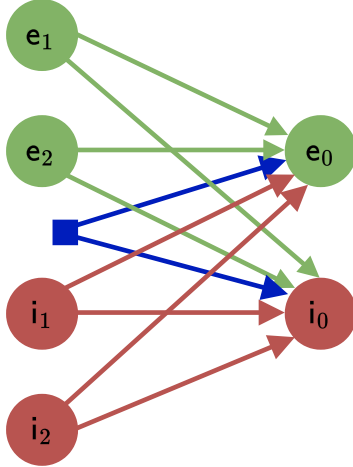


FIG. 7. Representative motif selected for in-depth analysis. The network motif consists of a balanced configuration with $\tilde{N}_{ee_0} = \tilde{N}_{ei_0} = \tilde{N}_{ie_0} = \tilde{N}_{ii_0} = 2$. In this figure, (e_1, e_2) and (i_1, i_2) represent \bar{e} and \bar{i} the mean neighborhood shown in Fig. 5.

where the coefficients a_{cd} and b_{cd} are given explicitly in Appendix E. The substitution rule was confirmed to be true, but it is omitted due to its length. The following section investigates this motif's dynamical equations in depth.

V. HOW INHIBITION AFFECTS THE DYNAMICS

The role of inhibitory neurons in shaping brain dynamics is an active field of research [5, 45]. Here, we investigate whether inhibitory neurons fundamentally alter the dynamics of our model or exert only a modulatory effect. If the system is quasi-critical, we expect its core features to persist with some modification. Using Eqs.

(27) and (29), we construct phase diagrams to examine how inhibitory parameters influence stability of the various phases. While inhibition does not introduce qualitative changes, it expands the model's stable region. As inhibitory strength increases, the system becomes more stable, average activity decreases, and dynamical susceptibility is reduced. In the unstable regime, we observe chaotic dynamics, which inhibition can suppress. The model follows a distinctive route to chaos, characterized by marginally stable orbits, period doubling, and occasional seemingly intermittent bursts of chaos. When y_1 acts as an external periodic input, strong inhibition induces unstable periodic behavior in excitatory neurons with the same period but a seemingly $-\pi/2$ phase shift.

A. Establishing Phase Diagrams

We begin by computing the Jacobian of the dynamical map (MF equations), at the fixed points, and by analyzing its eigenvalues. A fixed point is stable if all eigenvalues have magnitude less than one, and unstable if any eigenvalue exceeds one in magnitude. The Jacobian terms are defined as

$$J_{ij} = \frac{\partial h_i(t+1)}{\partial h_j(t)},$$

where h_i and $h_j \in \{h \mid h = (x_1, \dots, x_{\tau_e}, y_1, \dots, y_{\tau_i})\}$.

The fixed points of $x_1(t)$, $y_1(t)$, and Eqs. (33) are computed with the system of equations

$$\begin{aligned} x_1^* &= (1 - \tau_e x_1^*) F[x_1^*, y_1^*, p_s, \dots], \\ y_1^* &= (1 - \tau_i y_1^*) G[x_1^*, y_1^*, p_s, \dots], \end{aligned} \quad (48)$$

Note that $1 - \sum_{i=1}^{\tau_n} h_i^* \rightarrow (1 - \tau_n h_1^*)$ since $h_1^* = h_i^*$ for a fixed point, so should be constant. An example Jacobian \mathbb{J} for $\tau_e = 3$ and $\tau_i = 3$, which has the same form for every motif, is represented by

$$\mathbb{J} = \begin{array}{c|ccccc|ccccc} & x_1 & x_2 & x_3 & y_1 & y_2 & y_3 \\ \hline x_1 & -F + \frac{\partial F}{\partial x_1} \cdot x_0(t) & -F & -F & \frac{\partial F}{\partial y_1} \cdot x_0(t) & 0 & 0 \\ x_2 & 1 & 0 & 0 & 0 & 0 & 0 \\ x_3 & 0 & 1 & 0 & 0 & 0 & 0 \\ \hline y_1 & \frac{\partial G}{\partial x_1} \cdot y_0(t) & 0 & 0 & -G + \frac{\partial G}{\partial y_1} \cdot y_0(t) & -G & -G \\ y_2 & 0 & 0 & 0 & 1 & 0 & 0 \\ y_3 & 0 & 0 & 0 & 0 & 1 & 0 \end{array} \quad (49)$$

We will use the motif from Fig. 7 to draw our phase diagrams. We are choosing that inhibitor neurons always inhibit.

B. Nonequilibrium Phase Diagram and the Widom Line

Our phase diagram is a graphical representation that shows how the state of our dynamical system changes as a

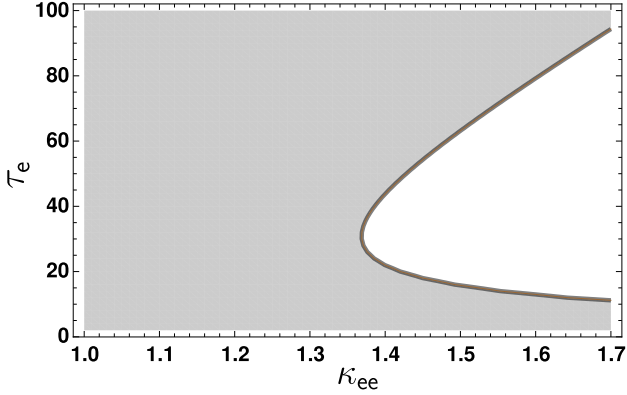


FIG. 8. Stability of solutions in the representative motif. A cross-section of the phase diagram showing the stability of the solutions of the excitatory activity $x_1(t)$ and the inhibitory activity $y_1(t)$ for the representative motif in Fig. 7. The x-axis represents the coupling strength between excitatory neurons (κ_{ee}), and the y-axis represents the refractory period of excitatory neurons (τ_e). The gray region corresponds to a stable nonzero fixed point, while the white region indicates an oscillatory phase with unstable fixed points. The solid black line marks the stability phase boundary, which is non-analytical. The remaining parameters are $\kappa_{ii} = \kappa_{ie} = \kappa_{ei} = 1.6$, $p_s = 10^{-3}$, $\tau_i = 5$, and $\tilde{N}_{ee_0} = \tilde{N}_{ei_0} = \tilde{N}_{ie_0} = \tilde{N}_{ii_0} = 2$.

function of parameters such as κ_{ee} , κ_{ei} , κ_{ii} , κ_{ie} , τ_e , τ_i , p_s , and the neighborhood sizes \tilde{N}_{ee_0} , \tilde{N}_{ie_0} , and \tilde{N}_{ei_0} , \tilde{N}_{ii_0} . For clarity and comparison with the purely excitatory model, we focus on a two-dimensional cross-section of this space, using κ_{ee} on the x-axis (excitatory-to-excitatory coupling strength) and τ_e on the y-axis (excitatory refractory period). To explore how inhibition affects the dynamics, we vary the inhibitory parameters κ_{ie} , κ_{ei} , κ_{ii} , τ_i , and p_s , allowing us to examine their role in modulating stability and their relationship to the quasi-critical hypothesis.

We select parameters within the physical regime by ensuring that all probabilities are well-defined, with the upper bound given in Eq. (2). Using the representative motif in Fig. 7, we solve Eq. (48) to find fixed points and assess their stability.

The representative phase diagram in Fig. 8 shows the stability of the solutions to Eqs. (46) and (47) for the motif in Fig. 7. It reveals a phase transition across a boundary separating stable and unstable fixed points. While qualitatively similar to the purely excitatory case, the stability boundary is shifted rightward, toward higher values of κ_{ee} , indicating that inhibition expands the stable region of the phase space. Inhibitory neurons thus serve as regulators, enhancing stability and allowing a broader range of configurations to remain dynamically stable. Varying the inhibitory parameters confirms that, in most cases, stronger inhibition shifts the stability boundary toward higher κ_{ee} values and reduces the mean excitatory activity. This effect is more pronounced at lower τ_e and higher κ_{ee} values. An exception occurs at low refractory periods (e.g., $\tau_e = 2$), where in-

creasing inhibition can shift the stable region leftward to lower κ_{ee} values, even as excitatory activity continues to decline.

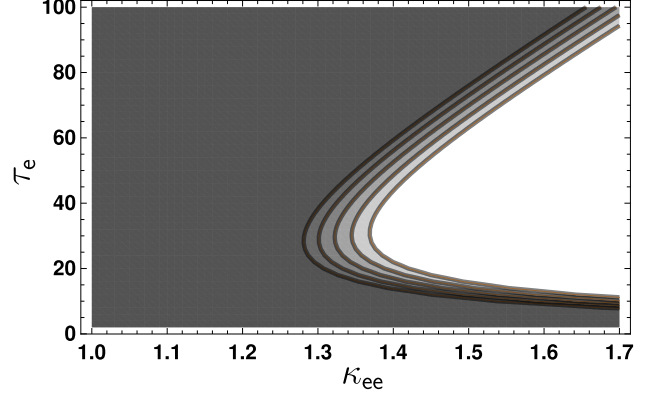


FIG. 9. Effect of inhibitory-to-excitatory coupling on phase stability. A cross-section of the phase diagram showing the stability of the solutions of the excitatory activity $x_1(t)$ and the inhibitory activity $y_1(t)$ for the representative motif in Fig. 7, as the coupling strength from inhibitory to excitatory neurons (κ_{ie}) increases from 0 to 1.6 in steps of .4 (left to right, darker to lighter gray). The gray regions indicate stable fixed-point phases, while the white region corresponds to an oscillatory phase with unstable fixed points. The x-axis represents the coupling strength between excitatory neurons (κ_{ee}), and the y-axis represents the refractory period of excitatory neurons (τ_e). Solid black lines denote stability phase boundaries. The other parameters are $\kappa_{ii} = \kappa_{ei} = 1.6$, $p_s = 10^{-3}$, $\tau_i = 5$, and $\tilde{N}_{ee_0} = \tilde{N}_{ei_0} = \tilde{N}_{ie_0} = \tilde{N}_{ii_0} = 2$.

We begin by exploring how varying κ_{ie} affects the phase diagram, as shown in Fig. 9. As κ_{ie} increases, the stability boundary shifts toward higher κ_{ee} , indicating increased stability. Stronger inhibition reduces excitatory activity, especially at low τ_e , expanding the stable region. On average, higher κ_{ie} reduces inhibitory activity due to fewer active excitatory neurons. An exception occurs at $\tau_e = 2$, where the boundary shifts leftward, though excitatory activity still decreases.

Importantly, shifts in the phase transition boundaries only occur when both $\kappa_{ei} \neq 0$ and $\kappa_{ie} \neq 0$. If either is zero, the Jacobian's upper-left and lower-right submatrices decouple, preventing inhibitory-excitatory interaction and eliminating the effect on stability.

Next, we examine how varying κ_{ei} affects the phase diagram, shown in Fig. 10. The diagrams resemble those for varying κ_{ie} , but changes in κ_{ei} shift the stability boundary less to the right for values up to about 1.6, where the shifts become comparable. Increasing κ_{ei} expands the stable region by enhancing excitatory input to inhibitory neurons, thereby increasing inhibitory activity and suppressing excitatory activity. This increase in average inhibitory activity produces a more pronounced and wider shift across τ_e values compared to varying κ_{ie} . At $\tau_e = 2$, the stability boundary shifts leftward with decreased excitatory activity. Fixing either κ_{ie} or κ_{ei} at

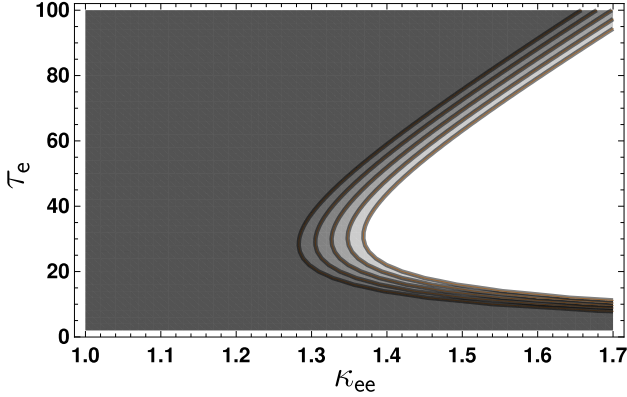


FIG. 10. Effect of excitatory-to-inhibitory coupling on phase stability. A cross-section of the phase diagram showing the stability of the solutions of the excitatory activity $x_1(t)$ and the inhibitory activity $y_1(t)$ for the representative motif in Fig. 7, as the coupling strength from excitatory to inhibitory neurons (κ_{ei}) increases from 0 to 1.6 in steps of .4 (left to right, darker to lighter gray). The gray regions correspond to stable fixed-point phases, while the white region indicates an oscillatory phase with unstable fixed points. The x-axis represents the coupling strength between excitatory neurons (κ_{ee}), and the y-axis represents the refractory period of excitatory neurons (τ_e). Solid black lines denote the stability phase boundaries. The other parameters are $\kappa_{ii} = \kappa_{ie} = 1.6$, $p_s = 10^{-3}$, $\tau_i = 5$, and $\tilde{N}_{ee_0} = \tilde{N}_{ei_0} = \tilde{N}_{ie_0} = \tilde{N}_{ii_0} = 2$.

a larger value (here, 1.6) amplifies the effect of increasing the other parameter on the phase transition boundary.

As τ_i increases, the phase diagram shifts left toward lower κ_{ee} values, indicating reduced stability (Fig. 11). This occurs because a longer inhibitory refractory period reduces the number of active inhibitory neurons, leading to increased excitation and diminished inhibitory regulation, which limits stability. An exception appears at $\tau_e = 2$, where stability shifts rightward toward higher κ_{ee} values, reflecting increased stability. For the inhibitory self-coupling parameter κ_{ii} , values of $\tau_e > 3$ show minimal impact on the stability boundary, so the corresponding plot is omitted. However, at $\tau_e = 2, 3$, increasing κ_{ii} shifts the stable region rightward, enhancing stability. This is accompanied by a slight increase in average excitation and a decrease in average inhibition. Overall, increasing inhibitory effectiveness generally expands the stable region of the phase diagram.

For completeness, we show in Fig. 12 that increasing p_s shifts the stability boundary toward higher values of κ_{ee} , particularly at larger τ_e . At low κ_{ee} values, the stability boundary remains unchanged. This indicates that higher p_s is needed to maintain stability as τ_e increases, consistent with observations in the purely excitatory case [13]. Additionally, increasing p_s elevates both excitatory and inhibitory activity levels.

For Eqs. (46) and (47), there are four solution pairs for the fixed points for x_1^* and y_1^* . The valid pair varies across the domain, except at $p_s = 0$, where two physical

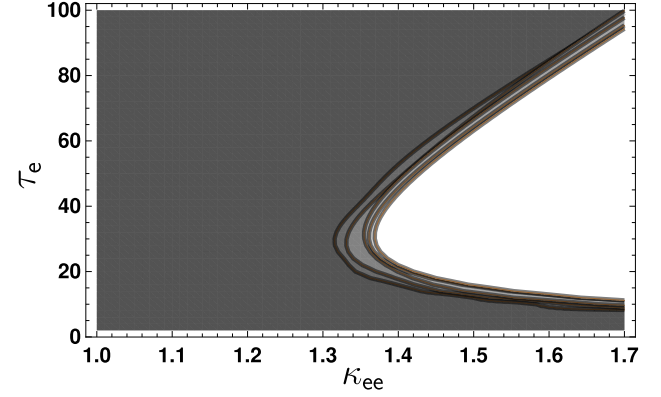


FIG. 11. Effect of inhibitory refractory period on phase stability. A cross-section of the phase diagram showing the stability of the solutions of the excitatory activity $x_1(t)$ and the inhibitory activity $y_1(t)$ for the representative motif in Fig. 7, as the inhibitory refractory period τ_i decreases from 100, 50, 25, 10, to 5 (left to right, darker to lighter gray). The gray regions indicate stable fixed-point phases, while the white region corresponds to an oscillatory phase with unstable fixed points. The x-axis represents the coupling strength between excitatory neurons (κ_{ee}), and the y-axis represents the refractory period of excitatory neurons (τ_e). Solid black lines denote the stability phase boundaries. The other parameters are $\kappa_{ii} = \kappa_{ie} = \kappa_{ei} = 1.6$, $p_s = 10^{-3}$, and $\tilde{N}_{ee_0} = \tilde{N}_{ei_0} = \tilde{N}_{ie_0} = \tilde{N}_{ii_0} = 2$.

pairs exist: one vanishing stable fixed point for $\kappa_{ee} < 1$, and one unstable non-vanishing fixed point for $\kappa_{ee} \geq 1$. Thus, $\rho_1^e(t)$ behaves like a Landau order parameter with κ_{ee} as the control parameter.

There is a disordered phase for $\kappa_{ee} \leq 1$ and an ordered phase for $\kappa_{ee} \geq 1$, separated by a second-order phase transition (Fig. 13). We have $\rho_1^e(t) = 0$ for $\kappa_{ee} \leq 1$ and $\rho_1^e(t) > 0$ for $\kappa_{ee} > 1$, with critical point $\kappa_{ee,c} = 1$. Expanding x_1^* near this critical point and $p_s = 0$ via a two-variable Taylor series shows a critical exponent $\beta = 1$: $x_1^* \propto (\kappa_{ee} - \kappa_{ee,c})^\beta$ for $\kappa_{ee} > 1$. Using $x_1^* \propto (\kappa_{ee} - \kappa_{ee,c})^1$ we found $\beta = 1$: $y_1^* \propto (\kappa_{ee} - \kappa_{ee,c})^\beta$ for $\kappa_{ee} > 1$. This exponent β matches that of the excitatory-only model [13] and coincides with the MF directed percolation universality class.

We can compute the dynamical susceptibility for the GCBM as follows

$$\chi_n = \lim_{p_s \rightarrow 0} \frac{\partial h_1^*}{\partial p_s},$$

$$\frac{\partial h_1^*}{\partial p_s} = \frac{\partial}{\partial p_s} (1 - \tau_n h_1^*) R[x_1^*, y_1^*, p_s, \dots],$$

where $R[x_1^*, y_1^*, p_s, \dots] = F[x_1^*, y_1^*, p_s, \dots]$ for χ_e , and $R[x_1^*, y_1^*, p_s, \dots] = G[x_1^*, y_1^*, p_s, \dots]$ for χ_i . After computing the susceptibility, and using the critical exponents of x_1^* and y_1^* , the susceptibility diverges at $\kappa_{ee,c}$ with exponent $\gamma' = 1$ for $\kappa_{ee} < 1$ as $\chi_{e,i} \propto (\kappa_{ee,c} - \kappa_{ee})^{-\gamma'}$, and for $\kappa_{ee} > 1$ with exponent $\gamma = 1$ as $\chi_{e,i} \propto (\kappa_{ee} - \kappa_{ee,c})^{-\gamma}$. These exponents match MF directed percolation and

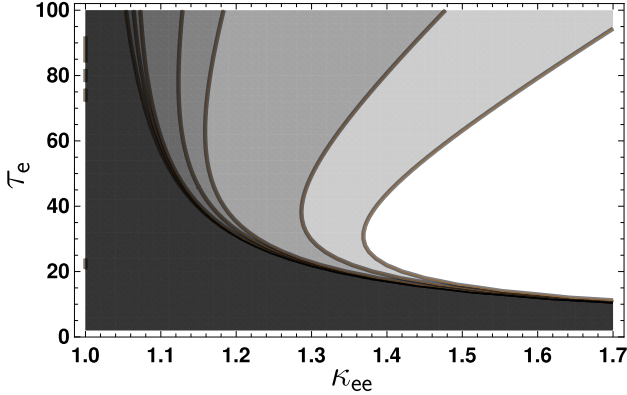


FIG. 12. Effect of spontaneous activation probability p_s on phase stability. A cross-section of the phase diagram showing the stability of the solutions of the excitatory activity $x_1(t)$ and the inhibitory activity $y_1(t)$ for the representative motif in Fig. 7, as p_s increases uniformly from left to right: 0, 0.5×10^{-5} , and 1×10^{-3} (darker to lighter gray). The gray regions represent stable fixed-point phases, while the white region corresponds to an oscillatory phase with unstable fixed points. The x-axis denotes the coupling strength between excitatory neurons (κ_{ee}), and the y-axis denotes the refractory period of excitatory neurons (τ_e). Solid black lines indicate the stability phase boundaries. The other parameters are $\kappa_{ii} = \kappa_{ie} = \kappa_{ii} = 1.6$, $\tau_i = 5$, and $\tilde{N}_{ee_0} = \tilde{N}_{ie_0} = \tilde{N}_{ii_0} = 2$.

agree with the excitatory-only model for both χ_e and χ_i [13]. Calculations used a simplified motif with one incoming connection per neuron type ($\tilde{N}_{ee_0} = \tilde{N}_{ie_0} = \tilde{N}_{ii_0} = 1$) due to complexity; for purely excitatory neurons, increasing neighbors does not change exponents, as expected.

For fixed τ_e and nonzero p_s , the peak susceptibility defines a nonequilibrium Widom line in the τ_e - κ_{ee} plane. Fig. 13 shows susceptibility curves for various p_s and τ_e , with red dots marking maximum susceptibility (log-scaled size) and red whiskers indicating full width at half maximum. For $\tau_e = 2$, the susceptibility peaks at a quasi-critical point $\kappa_{ee} = 1$, defining a Widom line in the p_s - κ_{ee} plane (inset Fig. 14). The maximum susceptibility decreases as p_s increases, analogous to a magnetic field in the Ising model. Compared to the CBM, the GCBM shows reduced susceptibility peaks but similar shape, indicating correlation functions decrease with added inhibition [46]. This reduction broadens the full width at half max, theoretically widening the susceptibility peak, thereby enlarging the quasi-critical region [47].

C. Chaotic Dynamics

Using the CBM with only excitatory neurons and the simplest parameters ($\tilde{N}_{ee_0} = 1$, $\tau_e = 2$), a period-doubling route to chaos emerges at the instability line as κ_{ee} increases, starting with period-four dynamics [48]. However, these chaotic dynamics occur in the non-physical regime where $\kappa_{ee} > \kappa_{ee}^{\max}$ (Eq. (2)). For $\tau_e \geq 2$,

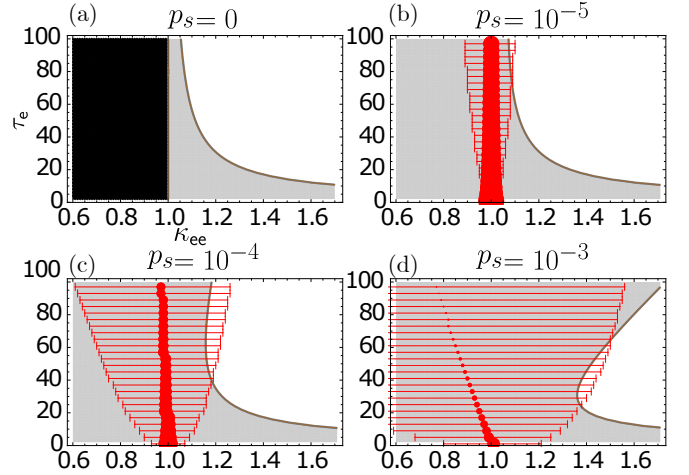


FIG. 13. (Color online) Nonequilibrium MF phase diagram with maximum susceptibility for select values of the probability of spontaneous activation p_s . The black region represents a subcritical disordered phase characterized by a vanishing fixed point. The gray regions correspond to a nonzero stable fixed-point phase, while the white region denotes a quasiperiodic oscillatory phase with unstable fixed points. The solid black line indicates a stability boundary. Red dots mark the locations of maximum susceptibility across κ_{ee} for each value of τ_e ; the size of each dot is scaled logarithmically with the magnitude of the dynamical susceptibility. Red whiskers represent the full width at half maximum. The other parameters are $\kappa_{ii} = \kappa_{ie} = \kappa_{ii} = 1.6$, $\tau_i = 5$, and $\tilde{N}_{ee_0} = \tilde{N}_{ie_0} = \tilde{N}_{ii_0} = 2$.

$\tilde{N}_{ee_0} \geq 1$, or with inhibition, a *marginally stable region* appears beyond the stability boundary. Increasing κ_{ee} eventually leads to period-doubling bifurcations and chaos. Although chaos typically lies outside the physical regime, sufficiently high \tilde{N}_{ee_0} and τ_e can bring it into the physical regime with or without inhibition, though adding inhibition generally delays the onset of chaos, allowing more non-chaotic dynamics. These biologically realistic parameters are computationally costly, but we provide examples demonstrating physical chaos. Such chaos under realistic conditions is relevant for understanding epileptic seizures, where chaotic transitions may underlie abrupt neural changes [31, 32]. Incorporating inhibitory neurons and additional parameters confirms a richer chaotic dynamics consistent with this route to chaos.

Generally, determining whether a system's dynamics is chaotic is challenging, as no universal definition exists. A commonly used method for identifying chaos is to test sensitivity to initial conditions by computing the largest Lyapunov exponent (LLE), $\lambda(\vec{x}_0)$. Specifically, $\lambda(\vec{x}_0) < 0$ indicates periodic behavior, $\lambda(\vec{x}_0) = 0$ corresponds to a marginally stable orbit, and $\lambda(\vec{x}_0) > 0$ suggests instability or chaos [49]. This approach was used in the previous analysis for the excitatory-only case. The calculation of the LLE for $\vec{x}(t+1)$ is detailed in Appendix F.

Our goal is to explore new dynamics by incorporating

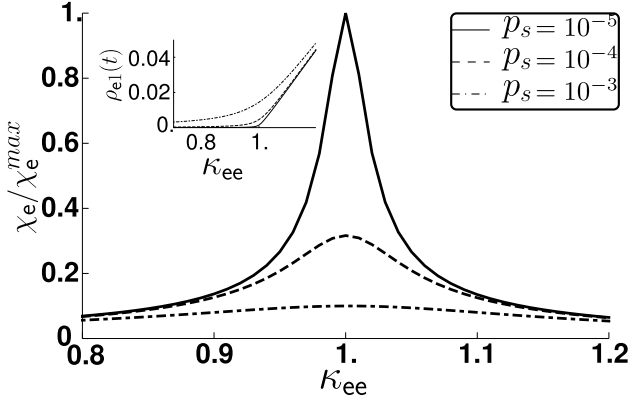


FIG. 14. Dynamical susceptibility χ_e of the excitatory neurons activity ρ_1^e , as a function of the excitatory coupling strength κ_{ee} , normalized by the maximum value of χ_e . The inset shows the average firing density of excitatory neurons, ρ_1^e , as a function of the excitatory coupling strength κ_{ee} . The dynamical susceptibility is normalized to the quasi-critical point at $\kappa_{ee} = 1$ for $p_s = 10^{-5}$. The other parameters are $\kappa_{ii} = \kappa_{ie} = \kappa_{ei} = 1.6$, $\tau_i = 2$, $\tau_e = 2$, and $\tilde{N}_{ee0} = \tilde{N}_{ei0} = \tilde{N}_{ie0} = \tilde{N}_{ii0} = 2$.

biologically realistic parameters like inhibition and provide further evidence for chaos using additional methods. Besides computing the LLE, we visualize attractors via time-delay embedding of $x_1(t)$, compute its discrete Fourier transform, and analyze the full Lyapunov spectrum [50]. This enables estimating the Lyapunov dimension, approximating the fractal dimension of strange attractors [51], implemented in Mathematica [52] as detailed in Appendix F. While the LLE is computed across parameters, we focus on κ_{ee} for comparison with the basic CBM (Fig. 15 (a)). Near unstable fixed points, dynamics become computationally challenging, appearing to slowly converge to periodic behavior—for example, at $\kappa_{ee} = 3$, values stabilize to 10^{-6} after 10^8 iterations.

We tested a non-exhaustive set of parameters, including excitatory-only networks, added inhibition, neighborhood connectivities ($\tilde{N}_{ee0} = 1$ or 2), delays ($\tau_e = 2$ or 3), and synaptic strengths (p_s), summarized in Figs. 15 and 16. Using more biologically realistic parameters—excitatory and inhibitory neurons with $\tilde{N}_{ee0} = \tilde{N}_{ei0} = \tilde{N}_{ie0} = \tilde{N}_{ii0} = 2$, $\tau_e = 3$, and $p_s = 10^{-3}$, we observed the LLE shown in Fig. 16. The first region where the LLE nears zero corresponds to the second-order phase transition (e.g., $\kappa_{ee} = 1$, $p_s = 0$), with further zeros indicating marginal stability, bifurcations, and chaos onset in Fig. 15 (a). In Figs. 15 and 16, solid black lines mark marginal stability points (bifurcations or onset of marginally stable regions), while dashed lines approximate their boundaries.

Figure 15 (b) illustrates the basic excitatory model with $\tilde{N}_{ee0} = 1$ and $p_s = 0$, comparing $\tau_e = 2$ (black) to $\tau_e = 3$ (red). Increasing τ_e introduces a marginally stable region rather than a single marginally stable point.

For $\tau_e = 3$, the first marginally stable point occurs at $\kappa_{ee} = 2.5$, compared to $\kappa_{ee} = 3$ for $\tau_e = 2$. Additionally, chaotic dynamics emerge earlier for $\tau_e = 3$. For marginally stable orbits, we find that the LLE is generally positive but converges to zero with increasing iterations, requiring at least 10^6 iterations in the studied cases. Figure 15 (c) shows the impact of increasing $\tilde{N}_{ee0} = 1$ (black) to $\tilde{N}_{ee0} = 2$ (red). This modification introduces a marginally stable region for higher values of κ_{ee} , along with new chaotic regions. Figure 15 (d) incorporates inhibition into the CBM model, revealing that while the dynamics occur at similar values of κ_{ee} , the unstable fixed point occurs later, and chaotic dynamics emerges earlier. Including inhibition also introduces a marginally stable region, similar to the excitatory-only cases. Interestingly, for $p_s < 10^{-3}$, the effect on marginally stable points is minimal, except at $\kappa_{ee} = 1$, where a non-zero p_s disrupts the phase transition.

Incorporating biologically realistic parameters still yields marginally stable regions and chaotic dynamics at higher κ_{ee} values (Fig. 16). With added parameters, doubling routes to chaos—beginning with finite-period windows—remain visible but occur after the marginally stable region rather than immediately following the unstable fixed point, as shown in Fig. 16 (a). Additional parameters also introduce new doubling routes with varying κ_{ee} widths, such as region B in Fig. 16 (b). In contrast, region A shows an abrupt transition from periodic to chaotic behavior without a clear route to chaos. Though narrow period-doubling windows may exist, they are undetectable within 10^{-6} precision in κ_{ee} . Small negative dips in the LLE within marginally stable regions quickly return to zero.

The marginally stable region appears nearly periodic in the solution plots of $x_1(t)$ and $y_1(t)$ from the map (Fig. 17), though the trajectory never exactly repeats, raising the question of chaos. To better distinguish marginally stable, periodic, and chaotic regimes, we computed time-delay embeddings and discrete Fourier transforms of $x_1(t)$, shown in Fig. 18 using the same parameters as Fig. 16. The left column (a–c) shows time-delay embeddings, and the right column (d–f) shows the single-sided amplitude spectra, corresponding respectively to the marginally stable ($\kappa_{ee} = 4.0$), periodic ($\kappa_{ee} = 4.5$), and chaotic ($\kappa_{ee} = 4.95$) regimes. Together, these visualizations offer a complementary view beyond the LLE for characterizing system dynamics.

The marginally stable region shows a deformed elliptical time-delay embedding and broad peaks in the Fourier spectrum (Fig. 16 (a,d)). The periodic regime displays a finite number of points in the time-delay embedding and half as many sharp, nonzero peaks in the one-sided Fourier spectrum; for example, Fig. 16 (b,e) shows a period-6 orbit with 6 distinct points in the embedding and 3 peaks at $1/6$, $1/3$, and $1/2$ Hz. In contrast, the chaotic regime is characterized by either a self-wrapping deformed ellipse or an infinite sequence of bifurcations in the embedding, along with a broadband Fourier spec-

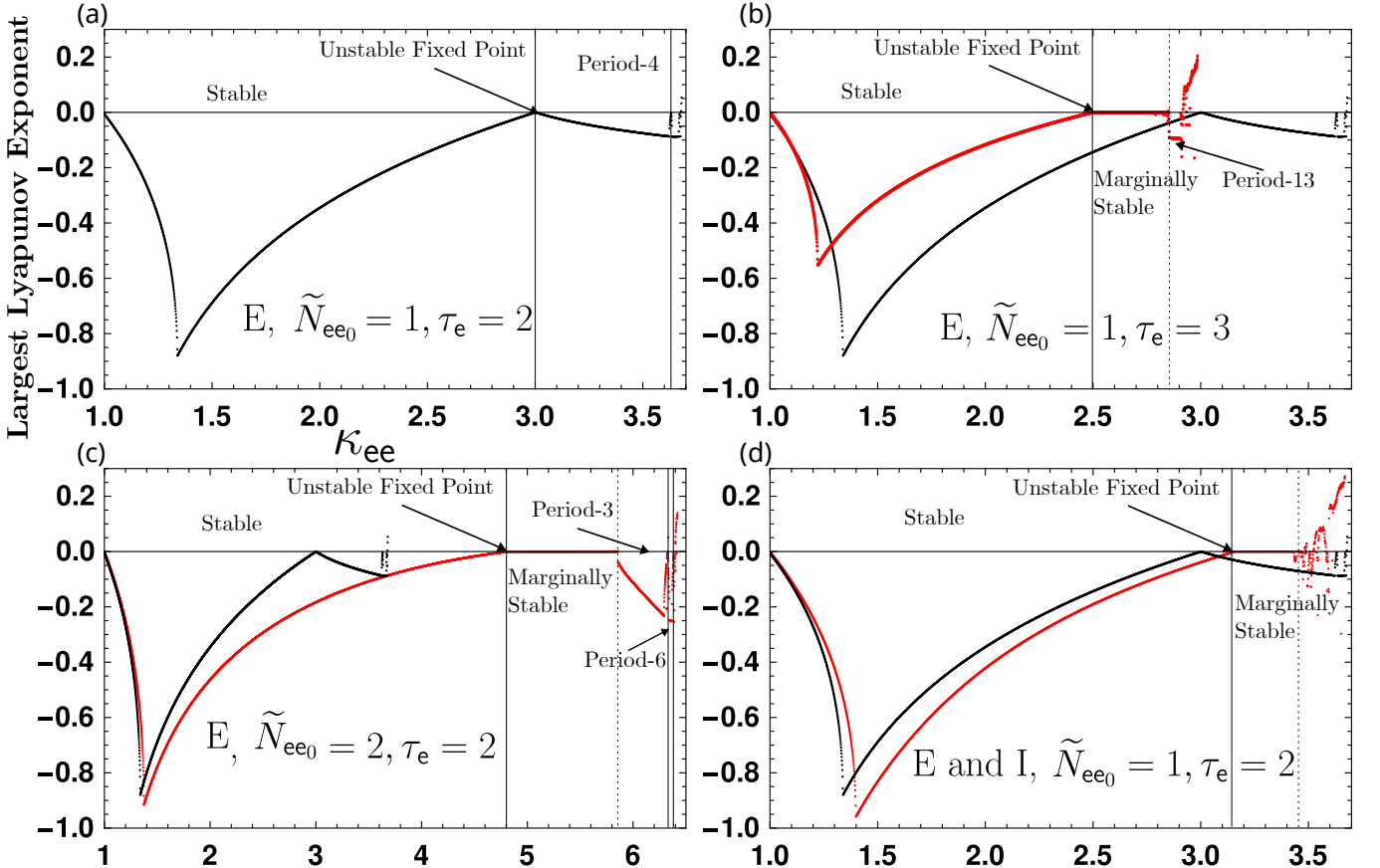


FIG. 15. (Color Online) Largest Lyapunov exponent (LLE) $\lambda(\vec{x}_0)$ of the excitatory activity $x_1(t)$ as a function of the excitatory coupling strength κ_{ee} . Panel (a) shows the basic excitatory model (E) with the number of excitatory neighbors of the representative excitatory neuron $\tilde{N}_{ee0} = 1$, the refractory period of the representative excitatory neuron $\tau_e = 2$, and the probability of spontaneous activity $p_s = 0$ (black). Panels (b), (c), and (d) contrast different variations of the excitatory-only model (E) in red, with the excitatory-only model (black) for comparison: Panel (b) shows the effect of increasing refractory period τ_e from 2 to 3, Panel (c) shows the effect of increasing number of excitatory neighbors \tilde{N}_{ee0} from 1 to 2, Panel (d) shows the inclusion of inhibition (I) in the model. Black vertical lines indicate the locations of unstable fixed points, followed by bifurcation points labeled with the emerging period. The dashed black line marks the approximate end of the marginally stable region.

trum (Fig. 16 (c,f)). While time-delay embeddings for marginally stable and chaotic regimes may appear similar, their Fourier spectra differ markedly. Within the marginally stable region, increasing κ_{ee} introduces additional frequencies in the Fourier spectrum of $x_1(t)$, consistent with a period-doubling route to chaos.

The delay embedding in Fig. 18 (c) forms a strange attractor, as evidenced by its fractional Lyapunov dimension [53]. The Lyapunov dimension D_L is computed from the Lyapunov spectrum of $\vec{x}(t+1)$ using the procedure described in Appendix F, following Ref. [52]. According to the Kaplan–Yorke conjecture, the Lyapunov dimension is defined as

$$D_L = j + \frac{\sum_{i=1}^j \lambda_i}{|\lambda_{j+1}|}. \quad (50)$$

With the Lyapunov exponents ordered from largest to smallest $\lambda_1 \geq \lambda_2 \geq \dots \geq \lambda_n$. Then, j is defined by the

largest index such that the following conditions hold

$$\sum_{i=1}^j \lambda_i \geq 0, \quad \text{and} \quad \sum_{i=1}^{j+1} \lambda_i < 0.$$

For Fig. 18 (c) $D_L = 1.02433$ with $j = 1$, which is a fractional dimension, meaning it is a strange attractor. In general, $1 \leq D_L \leq 2$ for each variation computed.

So far, our analysis of chaos has focused on the non-physical regime, where $\kappa_{ee} > \kappa_{ee}^{\max}$. However, by fixing $B = 0.5$ and choosing $\tau_e = 40$, $\tilde{N}_{ee0} = 5$, $\tilde{N}_{ei0} = \tilde{N}_{ie0} = \tilde{N}_{ii0} = 1$, $\kappa_{ii} = \kappa_{ie} = \kappa_{ei} = 0.8$, $\tau_i = 2$, and $p_s = 0$, we observe chaos within the physical regime, where all coupling strengths satisfy $\kappa_{nn} < \kappa_{nn}^{\max}$. Among these parameters, τ_e and \tilde{N}_{ee0} appear to be the most critical for enabling chaos in the physical regime when B is held fixed. Notably, inhibition is not necessary for the emergence of chaos in this regime. We find that increasing τ_e to a sufficiently high value, 40 in this example, lowers

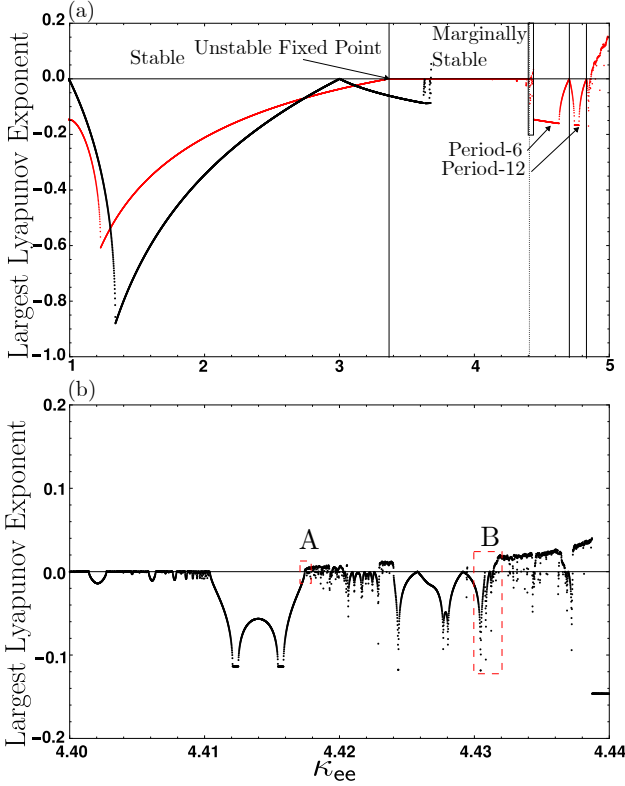


FIG. 16. (Color Online) (a) Largest Lyapunov exponent (LLE) $\lambda(\vec{x}_0)$ of the excitatory activity $x_1(t)$ as a function of κ_{ee} with parameters: $p_s = 10^{-3}$, $\tau_e = 3$, $\tau_i = 2$, $\tilde{N}_{ee_0} = \tilde{N}_{ei_0} = \tilde{N}_{ie_0} = \tilde{N}_{ii_0} = 2$. The solid black vertical lines mark, in sequence, the onset of instability (unstable fixed point) and subsequent bifurcations. The dashed black line indicates the approximate end of the marginally stable region. The black box in panel (a), starting at $\kappa_{ee} = 4.40$ shows the region magnified in panel (b). Label A marks a possible abrupt transition out of periodic behavior. Label B highlights a region consistent with period-doubling en route to chaos.

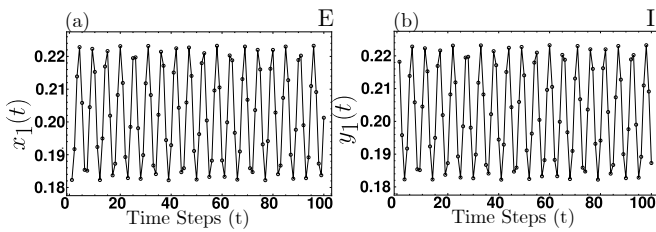


FIG. 17. Time series solutions in the marginally stable region of (a) the excitatory activity $x_1(t)$ and (b) the inhibitory activity $y_1(t)$, shown for the last 200 of 10^6 iterations. Parameters are: $\kappa_{ee} = 3.37$, $\kappa_{ii} = \kappa_{ie} = \kappa_{ei} = 1$, $p_s = 10^{-3}$, $\tau_e = 3$, $\tau_i = 2$, $B = 0.5$, and $\tilde{N}_{ee_0} = \tilde{N}_{ei_0} = \tilde{N}_{ie_0} = \tilde{N}_{ii_0} = 2$.

the minimal value of κ_{ee} required for chaos to appear in the physical regime, with chaos observed around $\kappa_{ee} = 2$. Additionally, setting $\tilde{N}_{ee_0} = 5$ ensures that $\kappa_{ee}^{\max} > 2.33$, thus maintaining the system within the physical regime. Interestingly, the range of Lyapunov exponents remains

largely unchanged for this parameter set. These values are illustrative rather than minimal, and merely demonstrate that chaos is indeed possible within the physical regime under suitable conditions.

1. Admissible Initial Conditions

It is necessary to find permissible initial conditions such that the maps define valid probabilities. Two criteria must be met: the probabilities for all possible states of $x_m(t)$ and $y_n(t)$ sum to one at all times, and each probability remains bounded between zero and one for all time shown in Eqs. (32). To determine the permissible initial conditions required to express Eqs. (32) in terms of the initial values only, we use Eqs. (27) and (29) together with the definitions of $x_0(t)$ and $y_0(t)$ given in Eq. (33), along with the following equations, which must be applied repeatedly

$$\begin{aligned} \sum_{m=1}^{\tau_e} x_m(t) &= \sum_{l=2}^t x_1(l) + \sum_{m=1}^{\tau_e-(t-1)} x_m(1), \\ \sum_{n=1}^{\tau_i} y_n(t) &= \sum_{l=2}^t y_1(l) + \sum_{n=1}^{\tau_i-(t-1)} y_n(1). \end{aligned} \quad (51)$$

We plotted cross-sections of the permissible initial conditions for different motifs with $\kappa_{ee} = 3.5$ and $\tilde{N}_{ee_0} = 2$, comparing excitatory-only (E) neurons and networks including inhibitory (I) neurons with refractory periods $\tau_e = 2$ or 15, as shown in Fig. 19. The permissible initial conditions were found by randomly sampling 10^5 points uniformly in the unit square $x_1(1), x_2(1) \in [0, 1]$, then plotting those (gray dots) that satisfy Eq. (32) up to time $t = 10^2$. We analytically solved Eqs. (32) and (51) up to $t = 4$, shown as black lines in Fig. 19; computations beyond $t = 4$ were neither feasible nor insightful. A strict upper bound constraint from $0 \leq \sum_{m=1}^{\tau_e} x_m(t) \leq 1$ at $t = 1$, restricts the permissible space maximally to the lower left triangle since $x_2(1) \leq 1 - x_1(1) - \sum_{m=3}^{\tau_e} x_m(1)$. Additional black lines appear sequentially at later times, further constraining the permissible initial conditions. Where appropriate we fixed $p_s = 0$, $\tilde{N}_{ie_0} = \tilde{N}_{ei_0} = \tilde{N}_{ii_0} = 2$, $x_3(1) = x_4(1) = \dots = x_{\tau_e}(1) = .01$, $\tau_i = 2$, $y_1(1) = y_2(1) = .01$, $\kappa_{ii} = \kappa_{ie} = \kappa_{ei} = 1.6$. Note that relaxing the constraints on $x_3(1)$ and $y_{1,2}(1)$ over $[0, 1]$ fills the previously inadmissible region of the lower-left triangle when projected onto the same axes.

D. CBM with an External Periodic Inhibitory Source

Experiments seem to indicate that inhibitory neurons exhibit periodic activation [54]. We can impose a periodic

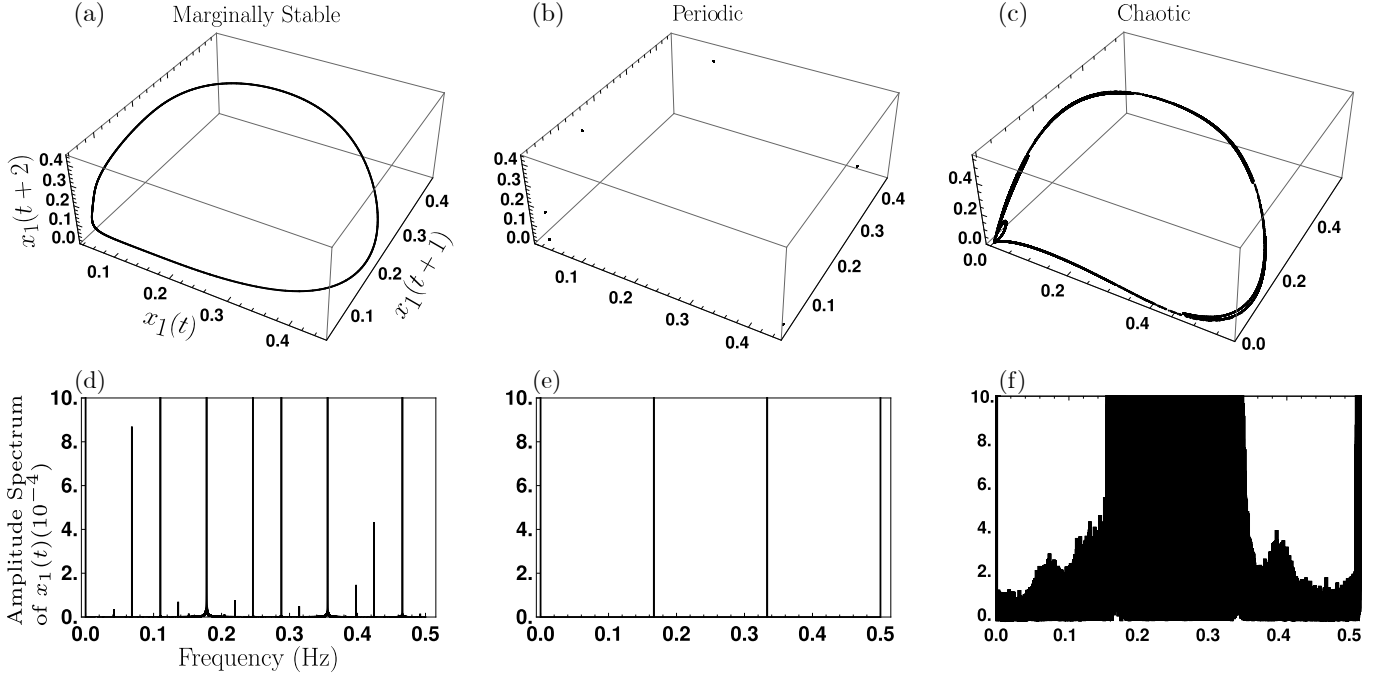


FIG. 18. Time-delay embeddings and Fourier spectra of $x_1(t)$. Upper row (a-c) is the time delay embedding of $x_1(t)$ and lower row (d-f) is the discrete Fourier transform of $x_1(t)$ with the single-sided amplitude being the y-axis. The columns correspond to the marginally stable region (a, d, $\kappa_{ee} = 4.0$), periodic region (b, e, $\kappa_{ee} = 4.5$), and chaotic region (c, f, $\kappa_{ee} = 4.95$). The other parameters are the same as Fig. 16: $\kappa_{ii} = \kappa_{ie} = \kappa_{ei} = 1$, $\kappa_{ee} = 1.6$, $p_s = 10^{-3}$, $\tau_e = 3$, and $\tau_i = 2$, $\tilde{N}_{ee0} = \tilde{N}_{ei0} = \tilde{N}_{ie0} = \tilde{N}_{ii0} = 2$.

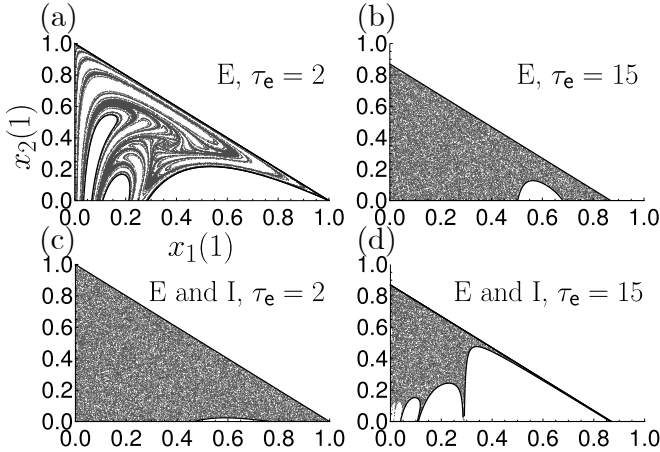


FIG. 19. Scatter plots of permissible initial conditions for $\kappa_{ee} = 3.5$ after 10^2 iterations. The black lines indicate analytical constraints derived from Eqs. (32), evaluated up to $t = 4$. Panels (a) and (b) show the CBM with $\tau_e = 2$ and $\tau_e = 15$, respectively. Panels (c) and (d) show the GCBM with the same corresponding τ_e values. All plots use $p_s = 0$, $\tilde{N}_{ee0} = 2$, and initial conditions $x_{3,\dots,\tau_e}(1) = 0.01$. The bottom row additionally includes: $\tilde{N}_{ie0} = \tilde{N}_{ei0} = \tilde{N}_{ii0} = 2$, $\tau_i = 2$, $y_{1,2}(1) = 0.01$, $\kappa_{ii} = \kappa_{ie} = \kappa_{ei} = 1.6$.

form on $y_1(t)$ in the MF approximation as

$$y_1(t) = D + A \sin^2 \left(\frac{\pi t}{T} \right), \quad (52)$$

choosing the square of the sine function to keep all values positive. This reduces the excitatory dynamics to that of a CBM driven by an external periodic inhibitory input. When $\kappa_{ie} = 0$, the periodic forcing of $y_1(t)$ does not affect the periodicity of $x_1(t)$'s solution, leaving the many-body CBM dynamics unchanged. We examine how imposing this periodic $y_1(t)$ alters $x_1(t)$'s dynamics by plotting $x_1(t)$ for varying κ_{ie} and fixed $\kappa_{ee} = 1.36, 1.37, 1.39, 1.60$, each exhibiting distinct behaviors (Fig. 20). For illustration, we choose $D = 0.05$, $A = 0.1$, and $T = 10$. The dynamics of $x_1(t)$ depend sensitively on these parameters governing the periodic inhibitory input.

For $\kappa_{ee} = 1.36$, $x_1(t)$ starts in a stable fixed point region at $\kappa_{ie} = 0$; once $\kappa_{ie} > 0$, $x_1(t)$ transitions to a periodic phase (Fig. 20 (a)), becoming entrained to $y_1(t)$ with the same period. This periodic behavior occurs for small amplitudes of the periodic function $y_1(t)$ and small coupling κ_{ie} . At $\kappa_{ee} = 1.37$, $x_1(t)$ begins in a marginally stable phase when $\kappa_{ie} = 0$ and again shifts to the periodic phase with the same period as $y_1(t)$ for $\kappa_{ie} > 0$ (Fig. 20 (b)). For $\kappa_{ee} = 1.39$, values of $\kappa_{ie} \leq 0.1$ correspond to a marginally stable phase for $x_1(t)$, while $\kappa_{ie} > 0.1$ leads to periodic behavior matching $y_1(t)$'s period (Fig. 20 (c)). Finally, at $\kappa_{ee} = 1.6$, $x_1(t)$ remains marginally stable for $0 \leq \kappa_{ie} \leq 1.5$, transitioning to the periodic phase for $\kappa_{ie} > 1.5$ (Fig. 20 (d)). Figure 20 (e) summarizes these transitions by showing periodic regions in gray and non-periodic in white across values of κ_{ee} and τ_e as κ_{ie} increases from 0 to 1.6.

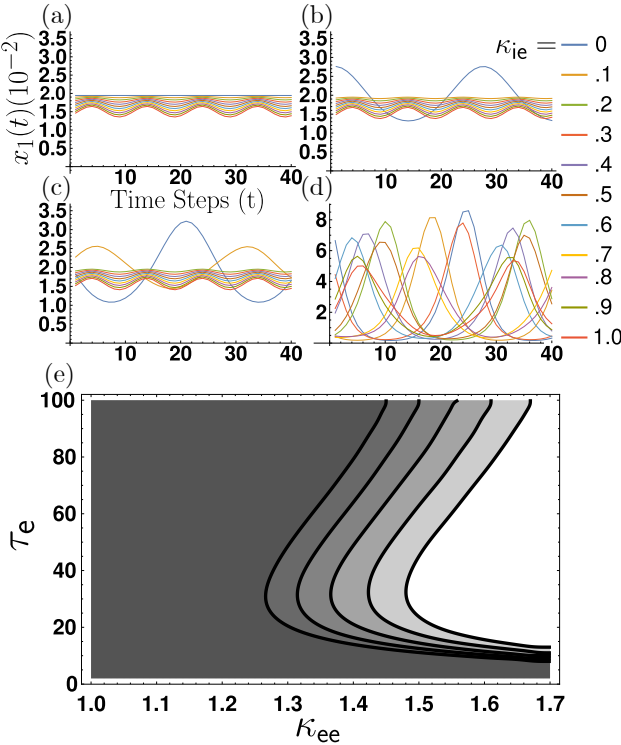


FIG. 20. (Color Online) Periodicity enslavement by an external periodic inhibitory source. (a-d) Time series plots of excitatory activity $x_1(t)$ with increasing κ_{ie} from 0 to 1 (as indicated in the legend) and $p_s = 10^{-3}$, $\tau_e = 15$. Each panel corresponds to a different excitatory coupling strength: $\kappa_{ee} = \{1.36, 1.37, 1.39, 1.60\}$ in panels (a), (b), (c), and (d), respectively. In panel (a), when $\kappa_{ie} = 0$, $x_1(t)$ settles into a stable fixed point; for $\kappa_{ie} > 0$, $x_1(t)$ becomes periodic and adopts the periodicity of the external inhibitory input $y_1(t)$. In panel (b), $x_1(t)$ starts in a marginally stable quasiperiodic regime and transitions to periodicity as κ_{ie} increases. In panel (c), $x_1(t)$ remains in a marginally stable quasiperiodic regime for $\kappa_{ie} \leq 0.1$ but transitions to periodic behavior for $\kappa_{ie} > 0.1$, enslaved by $y_1(t)$. In panel (d), all values of κ_{ie} maintain marginally stable quasiperiodic behavior. In panel (e), a plot distinguishing when $x_1(t)$ is periodic (gray) and when it is non-periodic (white) generally being marginally stable, as a function of κ_{ee} and κ_{ie} . κ_{ie} varies from 0 to 1.6 in steps of 0.4, with darker shades representing lower values. All panels use: $\tilde{N}_{ee_0} = 2$, $\tilde{N}_{ei_0} = 0$, $\tilde{N}_{ie_0} = 1$, and $\tilde{N}_{ii_0} = 0$.

This diagram differs from the phase diagrams since it only distinguishes whether the dynamics are periodic, not whether fixed points are stable. In the special case $\kappa_{ie} = 0$, it coincides with the CBM phase diagram for $\tilde{N}_{ee_0} = 2$. Originally, it is a phase diagram because the nonanalytic line separates stable fixed points (period-1 functions) from unstable ones. Notably, regions where $x_1(t)$ would normally be unstable fixed points become periodic when $y_1(t)$ is forced to be periodic. The extent of these changes depends on the parameters of the forced periodic $y_1(t)$.

VI. DISCUSSION

We developed a methodology for generating low-dimensional representations of functional networks using MF approximations. This framework was applied to a minimal neural dynamics model incorporating both excitatory and inhibitory neurons, in agreement with predictions of the quasi-criticality hypothesis.

We constructed a dictionary of fundamental rules for deriving MF equations across a range of network motifs. Our results demonstrate that the inclusion of inhibitory neurons generally promotes stability within the system. Additionally, we characterized chaotic dynamics in detail within the non-physical regime and identified examples within the physical regime. In both cases, we observed the emergence of a marginally stable region that transitions to chaos either via a period-doubling route or through an abrupt onset. These findings highlight the stabilizing influence of inhibition and elucidate the mechanisms underlying the transition to complex dynamics in neural networks.

Our findings support the quasi-criticality hypothesis by demonstrating that the system's maximum susceptibility decreases as the strength of the external drive increases, even with the inclusion of inhibitory neurons. Despite this modulation, the system remains within the directed percolation universality class, exhibiting a disorder-order phase transition when the probability of spontaneous activation vanishes. Inhibitory connections reshape the phase diagram by expanding the stable region: increasing inhibitory-to-excitatory (I→E) or excitatory-to-inhibitory (E→I) coupling strengths, weakening inhibitory-to-inhibitory (I→I) interactions, or shortening the inhibitory refractory period all enhance network stability. An exception occurs at very small values of the excitatory refractory period, τ_e , where the stable region contracts for reasons that remain unclear. Notably, these changes consistently reduce the average excitatory activity, highlighting the role of inhibition in maintaining the network near the quasi-critical regime. Furthermore, the addition of inhibitory neurons broadens the region of high susceptibility while lowering its peak values, suggesting that inhibition enables the system to remain sensitive across a wider parameter range. Although our framework does not capture temporal mutual information due to the absence of time-resolved activity, these results emphasize the critical role of inhibitory dynamics in stabilizing network activity and supporting quasi-critical behavior.

We have improved the classification of unstable regions exhibiting chaotic dynamics by incorporating more biologically realistic parameters into our model. Across most network configurations, beyond the simplest excitatory-only case, we consistently observed a sequence of dynamic regimes: a stable region, followed by a marginally stable region, which often transitions into chaos via a period-doubling route. Although chaos was primarily analyzed in the non-physical regime due to the

computational cost of simulations with physical parameters, we found no significant qualitative differences between the two. In some cases, we also observed a direct transition from marginal stability to chaos, though this pathway requires further investigation. To characterize chaotic behavior, we employed multiple analytical techniques, including the computation of the largest Lyapunov exponent, time-delay embedding, and discrete Fourier analysis of the average excitatory activity. A critical aspect of this analysis was the careful selection of permissible initial conditions to ensure accurate identification of chaotic regimes. Together, these results offer new insights into the rich dynamics of neural networks composed of both excitatory and inhibitory populations.

Our findings further support Ref. [13]’s hypothesis that oscillations in the quasiperiodic region may be linked to synchronizations observed during epileptic seizures [13, 55]. The presence of chaotic dynamics with more biologically realistic parameters in the unstable fixed-point region strengthens the potential connection between the unstable regime and epileptic seizures, which can also exhibit chaotic behavior [30, 31]. We found that forcing the inhibitory neuron activation density to be periodic induces periodic behavior in excitatory neurons with the same period and an approximate $-\pi/2$ phase shift, but only when the connection strength between inhibitory and excitatory neurons is sufficiently high. This threshold increases as the strength of the excitatory to excitatory connection grows. These findings may provide insights into how neurons could synchronize during an epileptic seizure.

A key motivation for our work is to identify a homeostatic mechanism that maintains the system within the quasi-critical regime, potentially mediated by inhibitory neurons. In addition, we aim to develop an experimentally measurable biomarker that indicates the system’s proximity to chaotic dynamics, offering insight into transitions toward instability. We envision that our model could help guide the design of such a biomarker, leveraging controlled manipulations of excitatory and inhibitory connectivity to assess network susceptibility and stability. Of particular interest is the application of this biomarker to real-time seizure prediction, providing clinical value for individuals with epilepsy, a direction we are actively pursuing.

Appendix A: Lists of symbols and notation used

- N_e : Number of Excitatory Neurons
- N_i : Number of Inhibitory Neurons
- e_μ : Excitatory Neurons
- i_ν : Inhibitory Neurons
- μ : Index of Excitatory Neurons
- ν : Index of Inhibitory Neurons
- n : Either Excitatory or Inhibitory Neuron
- $z_{e_\mu}(t)$: Excitatory Dynamical States Variable
- $z_{i_\nu}(t)$: Inhibitory Dynamical States Variable

- t : Time Index of State Variables
- $\mathcal{S} = \{\mathcal{S}_e, \mathcal{S}_i\}$: Set of Node States of Excitatory and Inhibitory Neurons
- τ_e : Refractory Period of Excitatory Neurons
- τ_i : Refractory Period of Inhibitory Neurons
- $z(t)$: Sequence of Individual Neuron States
- C : Configuration Space Neuron’s States
- Z : States of the Arcs (Signals Transmission)
- Z_n : State of Directed Edges for Spontaneous Activation
- $Z_{nn'}$: State of Directed Edges Two Vertices
- $Z_{ee'}$: State of Directed Edges Three Vertices
- $Z_e^{i_\nu}$: State of Directed Edges Two Vertices with External source
- P : Transmission Probabilities
- $P_{nn'}$: Probability of Transmission Two Vertices
- $P_{nn'}^{i_\nu}$: Probability of Transmission Three Vertices
- p_{su} : Probability of Spontaneous Activation for Excitatory Neurons
- p_{sv} : Probability of Spontaneous Activation for Inhibitory Neurons
- p_s : Probability of Spontaneous Activation when $p_{su} = p_{sv}$
- $k_{nn'}$: In Degree of Nodes
- $p_{nn'}^{nn'}$: Exponential Branching Decay Factor
- $\kappa_{nn'} \in \{\kappa_{ee}, \kappa_{ei}, \kappa_{ie}, \kappa_{ii}\}$: Branching Parameter
- $\kappa_{nn'}^{\max}$: Maximum Physical κ Value
- B : Bias Parameter
- \mathcal{N}_n : Neighborhood of Postsynaptic Neuron n
- \tilde{N}_{en} : Number of Excitatory Neighbors of Postsynaptic Neuron n
- \tilde{N}_{in} : Number of Inhibitory Neighbors of Postsynaptic Neuron n
- $\tilde{Z}_{e_\mu'}$: Sequence of All Excitatory Arc States of Postsynaptic Neuron e
- $\tilde{Z}_{i_\nu'}$: Sequence of All Inhibitory Arc States of Postsynaptic Neuron e
- $U(\tilde{Z}_{e'})$: Excitatory Site Activation Function
- $U(\tilde{Z}_{i'})$: Inhibitory Site Activation Function
- $\tilde{z}_{n'}(t)$: The Set of States of the Neighboring Neurons of Postsynaptic Neuron n'
- $W_{01}^n(\tilde{z}_{n_0}(t))$: Transition Probability from Quiescent (0) to Active (1) State
- $\overline{W_{01}^n}$: Transition Probability when All Neighbors are Active
- $A_0^{n_0}(t), A_\mu^{n_0}(t), B_\nu^{n_0}(t)$: Event Notation for the Dictionary
- $P(A_0^{n_0}(t)), P(A_\mu^{n_0}(t)), P(B_\nu^{n_0}(t))$: Probability of the Events for the Dictionary
- E_m^n : Probability of at least m Excitatory Arcs, targeted at n , are Simultaneously Active
- $I_{[m]}^n$: Probability of exactly m Inhibitory Arcs, targeted at n , are Simultaneously Active
- $\rho_1^e(t)$: Excitatory Density of Activation
- $\rho_1^i(t)$: Inhibitory Density of Activation
- $\bar{\rho}_1^n$: Time Average Densities
- N_T : Number of Iterations of the Map
- χ_n : Zero Field Dynamical Susceptibility

e_0 : Representative Excitatory Neuron
 i_0 : Representative Inhibitory Neuron
 $z_{n_0}(t)$: State of Representative Neuron
 $\tilde{z}_{n_0}(t)$: States of Neighborhood Neurons of Representative Neurons $z_{n_0}(t)$
 $x_m(t)$: Probability for an Excitatory Neuron to be in State m
 $y_n(t)$: Probability for an Inhibitory Neuron to be in State n
 J_{ij} : Jacobian Matrix
 x_1^* : Fraction of Active Excitatory Neurons' Fixed Point
 y_1^* : Fraction of Active Inhibitory Neurons' Fixed Point
 $\kappa_{ee,c}$: Critical κ_{ee} Value
 β : Critical exponent of Activation Density and κ_{ee}
 γ : Critical exponent of Susceptibility and κ_{ee}
 $\lambda(\vec{x}_0)$: largest Lyapunov exponent (LLE)
 D_L : Lyapunov Dimension

Appendix B: Complete Dictionary

We have previously established the MF dictionary for the case of arcs, but not for hyperarcs, which we now present here. We begin by explicitly defining the arc-activation probability function for each arc and hyperarc as

$$\begin{aligned}
 P(Z_{nn'}|z_n(t)) &= \delta_{1,z_{n_0}(t)}((1 - P_{nn'})\delta_{0,Z_{nn'}} + \\
 &\quad P_{nn'}\delta_{1,Z_{nn'}}) + (1 - \delta_{1,z_{n_0}(t)})(1 - Z_{nn'}(t)), \\
 P(Z_{ee'}^i|z_e(t)) &= \delta_{1,z_{i_0}(t)}((1 - P_{ee'}^i)\delta_{0,Z_{ee'}^i} + \\
 &\quad P_{ee'}^i\delta_{1,Z_{ee'}^i}) + (1 - \delta_{1,z_{i_0}(t)})(1 - Z_{ee'}^i(t)), \\
 P(Z_e^i|z_e(t)) &= \delta_{1,z_{i_0}(t)}((1 - P_e^i)\delta_{0,Z_e^i} + \\
 &\quad P_e^i\delta_{1,Z_e^i}) + (1 - \delta_{1,z_{i_0}(t)})(1 - Z_e^i(t)). \quad (B1)
 \end{aligned}$$

Starting from the MF equations, and substituting the transition probabilities $W_{01}^{e_0}(\tilde{z}_{e_0}(t))$ and $W_{01}^{i_0}(\tilde{z}_{i_0}(t))$ using Eq. (7), one can show that

$$\begin{aligned}
 F &= \sum_{\forall \tilde{Z}_{e_0}} U(\tilde{Z}_{e_0}) \cdot p_{se_\mu} \cdot \sum_{z_{e_1}(t)=0}^{\tau_e} P(Z_{e_1 e_0} | z_{e_1}(t)) \cdot x_{z_{e_1}(t)} \cdots \\
 &\quad \sum_{z_{i_1}(t)=0}^{\tau_i} P(Z_{e_1 i_0}^{i_1} | z_{i_1}(t)) \cdot y_{z_{i_1}(t)} \cdots \\
 &\quad \sum_{z_{i_1}(t)=0}^{\tau_i} P(Z_{i_1 e_0} | z_{i_1}(t)) \cdot y_{z_{i_1}(t)} \cdots, \quad (B2)
 \end{aligned}$$

$$\begin{aligned}
 G &= \sum_{\forall \tilde{Z}_{i_0}} U(\tilde{Z}_{i_0}) \cdot p_{si_\nu} \cdot \sum_{z_{e_1}(t)=0}^{\tau_e} P(Z_{e_1 i_0} | z_{e_1}(t)) \cdot x_{z_{e_1}(t)} \cdots \\
 &\quad \sum_{z_{i_1}(t)=0}^{\tau_i} P(Z_{i_1 i_0} | z_{i_1}(t)) \cdot y_{z_{i_1}(t)} \cdots. \quad (B3)
 \end{aligned}$$

With some algebra, and using the arc activation functions in Eq. (B1), the functions F and G can be written as follows

$$\begin{aligned}
 F &= \sum_{\forall \tilde{Z}_{e_0}} U(\tilde{Z}_{e_0}) \cdot p_{se_\mu} \cdot \prod_{\mu=1}^{\tilde{N}_{ee_0}} ((1 - P_{e_\mu e_0} x_1(t))\delta_{0,Z_{e_\mu e_0}} + \\
 &\quad P_{e_\mu e_0} x_1(t)\delta_{1,Z_{e_\mu e_0}}) \cdot \prod_{\forall e_\mu, i_\nu \in \tilde{N}_{ie_0}} ((1 - P_{e_\mu e_0}^i y_1(t))\delta_{0,Z_{e_\mu e_0}^i} + \\
 &\quad P_{i_\nu e_0} y_1(t)\delta_{1,Z_{i_\nu e_0}}) \cdot \prod_{\forall i_\nu \in \tilde{N}_{ie_0}} ((1 - P_{e_0}^{i_\nu} y_1(t))\delta_{0,Z_{e_0}^{i_\nu}} + \\
 &\quad P_{i_\nu e_0} y_1(t)\delta_{1,Z_{i_\nu e_0}}) \cdot \prod_{\nu=1}^{\tilde{N}_{ie_0}} ((1 - P_{i_\nu e_0} y_1(t))\delta_{0,Z_{i_\nu e_0}} + \\
 &\quad P_{i_\nu e_0} y_1(t)\delta_{1,Z_{i_\nu e_0}}), \quad (B4)
 \end{aligned}$$

$$\begin{aligned}
 G &= \sum_{\forall \tilde{Z}_{i_0}} U(\tilde{Z}_{i_0}) \cdot p_{si_\nu} \cdot \prod_{\mu=1}^{\tilde{N}_{ee_0}} ((1 - P_{e_\mu i_0} x_1(t))\delta_{0,Z_{e_\mu i_0}} + \\
 &\quad P_{e_\mu i_0} x_1(t)\delta_{1,Z_{e_\mu i_0}}) \cdot \prod_{\nu=1}^{\tilde{N}_{ie_0}} ((1 - P_{i_\nu i_0} y_1(t))\delta_{0,Z_{i_\nu i_0}} + \\
 &\quad P_{i_\nu i_0} y_1(t)\delta_{1,Z_{i_\nu i_0}}), \quad (B5)
 \end{aligned}$$

Starting with Eq. (7) can write the cases when all the nieghbors are active $\overline{W_{01}^{e_0}}$ and $\overline{W_{01}^{i_0}}$ as

$$\begin{aligned}
 \overline{W_{01}^{e_0}} &= \sum_{\forall \tilde{Z}_{e_0}} U(\tilde{Z}_{e_0}) \cdot p_{se_\mu} \cdot \prod_{\mu=1}^{\tilde{N}_{ee_0}} ((1 - P_{e_\mu e_0})\delta_{0,Z_{e_\mu e_0}} + \\
 &\quad P_{e_\mu e_0} \delta_{1,Z_{e_\mu e_0}}) \cdot \prod_{\forall e_\mu, i_\nu \in \tilde{N}_{ie_0}} ((1 - P_{e_\mu e_0}^i)\delta_{0,Z_{e_\mu e_0}^i} + \\
 &\quad P_{i_\nu e_0} \delta_{1,Z_{i_\nu e_0}}) \cdot \prod_{\forall i_\nu \in \tilde{N}_{ie_0}} ((1 - P_{e_0}^{i_\nu})\delta_{0,Z_{e_0}^{i_\nu}} + \\
 &\quad P_{i_\nu e_0} \delta_{1,Z_{i_\nu e_0}}) \cdot \prod_{\nu=1}^{\tilde{N}_{ie_0}} ((1 - P_{i_\nu e_0})\delta_{0,Z_{i_\nu e_0}} + \\
 &\quad P_{i_\nu e_0} \delta_{1,Z_{i_\nu e_0}}), \quad (B6)
 \end{aligned}$$

$$\begin{aligned} \overline{W_{01}^{i_0}} = & \sum_{\forall \tilde{Z}_{i_0}} U(\tilde{Z}_{i_0}) \cdot p_{s_{i_\nu}} \cdot \prod_{\mu=1}^{\tilde{N}_{e_{i_0}}} ((1 - P_{e_\mu i_0}) \delta_{0, Z_{e_\mu i_0}} + \\ & P_{e_\mu i_0} \delta_{1, Z_{e_\mu i_0}}) \cdot \prod_{\nu=1}^{\tilde{N}_{i_0}} ((1 - P_{i_\nu i_0}) \delta_{0, Z_{i_\nu i_0}} + \\ & P_{i_\nu i_0} \delta_{1, Z_{i_\nu i_0}}), \end{aligned} \quad (B7)$$

when the substitution rules in Eq. (34) are applied to $\overline{W_{01}^{e_0}}$ and $\overline{W_{01}^{i_0}}$, they yield expressions that are equivalent to F and G , respectively.

Appendix C: Transition probabilities $\overline{W_{01}^{n_0}}$ for the motif in Fig. 6

In Section IV, the solution of the transition probability $\overline{W_{01}^{e_0}}$ for the motif in Fig. 6 was already given, and now we will provide further details. This will be followed by showing the solutions for the other transition probabilities, starting with $\overline{W_{01}^{i_0}}$.

First, $\overline{W_{01}^{e_0}}$ is calculated from Eq. (16)

$$\overline{W_{01}^{e_0}} = E_1^{e_0} I_{[0]}^{e_0} + E_2^{e_0} I_{[1]}^{e_0},$$

where $E_1^{e_0} = S_1^{e_0} - S_2^{e_0}$ and $E_2^{e_0} = S_2^{e_0}$ are derived from Eq. (12). Equation (13) provides expressions for $S_1^{e_0} = P(A_0^{e_0}) + P(A_1^{e_0}) = p_s + P_{e_1 e_0}$ and $S_2^{e_0} = P(A_0^{e_0} \cap A_1^{e_0}) = p_s P_{e_1 e_0}$. Similarly, the terms $I_{[0]}^{e_0} = S_0^{e_0} - S_1^{e_0}$ and $I_{[1]}^{e_0} = S_1^{e_0}$, with $S_0^{e_0} = 1$ and $S_1^{e_0} = P(B_1^{e_0}) = P_{i_1 e_0}$, are obtained from Eqs. (14) and (15). Putting all the pieces together leads to Eq. (41).

One can follow a similar procedure to compute $\overline{W_{01}^{i_0}}$

$$\overline{W_{01}^{i_0}} = E_1^{i_0} I_{[0]}^{i_0},$$

where $E_1^{i_0} = S_1^{i_0} = P(A_0^{i_0}) = p_s$ and $I_{[0]}^{i_0} = S_0^{i_0} = 1$, with the result $\overline{W_{01}^{i_0}} = p_s$.

Appendix D: Dynamical equations of the motif in Fig. 6: An example proof of the substitution rule

To demonstrate the validity of the substitution rule for the example motif, it is necessary to compute the remaining transition probabilities $\overline{W_{01}^{e_0}} \neq \overline{W_{01}^{i_0}}$. These can be obtained from $\overline{W_{01}^{e_0}}$ by setting to zero the transmission-probability variables corresponding to inactive neighbors.

From Eq. (41)

$$\overline{W_{01}^{e_0}} = (p_s + (1 - p_s) P_{e_1 e_0})(1 - P_{i_1 e_0}) + p_s P_{e_1 e_0} P_{i_1 e_0},$$

one obtains

$$\begin{aligned} W_{01}^{e_0}((1; \mathcal{I})) &= p_s + (1 - p_s) P_{e_1 e_0}, \\ W_{01}^{e_0}((\mathcal{I}; 1)) &= p_s (1 - P_{i_1 e_0}), \\ W_{01}^{e_0}((\mathcal{I}; \mathcal{I})) &= p_s. \end{aligned}$$

We can now explicitly write $x_1(t+1)$ using Eqs. (27) and (33), together with the transition probabilities above, and after some algebraic manipulations obtain

$$\begin{aligned} \frac{x_1(t+1)}{x_0(t)} &= W_{01}^{e_0}((1; 1)) x_1(t) y_1(t) \\ &+ W_{01}^{e_0}((1; \mathcal{I})) x_1(t) (1 - y_1(t)) \\ &+ W_{01}^{e_0}((\mathcal{I}; 1)) (1 - x_1(t)) y_1(t) \\ &+ W_{01}^{e_0}((\mathcal{I}; \mathcal{I})) (1 - x_1(t)) (1 - y_1(t)) \\ &= (p_s + (1 - p_s) P_{e_1 e_0} x_1(t)) (1 - P_{i_1 e_0} y_1(t)) \\ &+ p_s P_{e_1 e_0} x_1(t) P_{i_1 e_0} y_1(t). \end{aligned} \quad (D1)$$

Similarly, for $\overline{W_{01}^{i_0}}$ the only neighbor is p_s so

$$\overline{W_{01}^{i_0}} = p_s. \quad (D2)$$

We can now explicitly write $y_1(t+1)$ using Eq. (29)

$$y_1(t+1) = y_0(t) p_s. \quad (D3)$$

We see that these dynamical equations match exactly those obtained via the substitution rule for the non-trivial equations in Eqs. (43), thereby providing an explicit example of the validity of the substitution rule.

Appendix E: Dynamical equations of the motif in Fig. 7

The dynamic maps expressed as a polynomial sum for the motif in Fig. 7 were given in Section IV, and here we provide the corresponding coefficients. The substitution rule used to compute these dynamical maps was verified to hold, but the full derivation is omitted here due to its length. The final expression for excitation is

$$x_1(t+1) = x_0(t) \sum_{c=0, d=0}^{\tilde{N}_{e_{i_0}}, \tilde{N}_{i_0}} a_{cd} x_1(t)^c y_1(t)^d, \quad (E1)$$

where

$$\begin{aligned} a_{00} &= p_s \\ a_{01} &= -p_s (P_{i_1 e_0} + P_{i_2 e_0}) \\ a_{02} &= p_s P_{i_1 e_0} P_{i_2 e_0} \\ a_{10} &= (1 - p_s) (P_{e_1 e_0} + P_{e_2 e_0}) \\ a_{11} &= (-1 + 2p_s) (P_{e_1 e_0} + P_{e_2 e_0}) (P_{i_1 e_0} + P_{i_2 e_0}) \\ a_{12} &= (1 - 3p_s) (P_{e_1 e_0} + P_{e_2 e_0}) P_{i_1 e_0} P_{i_2 e_0} \\ a_{20} &= (p_s - 1) P_{e_1 e_0} P_{e_2 e_0} \\ a_{21} &= (2 - 3p_s) P_{e_1 e_0} P_{e_2 e_0} (P_{i_1 e_0} + P_{i_2 e_0}) \\ a_{22} &= (2p_s - 1) 3 P_{e_1 e_0} P_{e_2 e_0} P_{i_1 e_0} P_{i_2 e_0}, \end{aligned} \quad (E2)$$

and, for inhibition,

$$y_1(t+1) = y_0(t) \sum_{c=0, d=0}^{\tilde{N}_{e_{i_0}}, \tilde{N}_{i_0}} b_{cd} x_1(t)^c y_1(t)^d, \quad (E3)$$

where

$$\begin{aligned}
b_{00} &= p_s \\
b_{01} &= -p_s(P_{i_1 i_0} + P_{i_2 i_0}) \\
b_{02} &= p_s P_{i_1 i_0} P_{i_2 i_0} \\
b_{10} &= (1 - p_s)(P_{e_1 i_0} + P_{e_2 i_0}) \\
b_{11} &= (-1 + 2p_s)(P_{e_1 i_0} + P_{e_2 i_0})(P_{i_1 i_0} + P_{i_2 i_0}) \\
b_{12} &= (1 - 3p_s)(P_{e_1 i_0} + P_{e_2 i_0})P_{i_1 i_0} P_{i_2 i_0} \\
b_{20} &= (p_s - 1)P_{e_1 i_0} P_{e_2 i_0} \\
b_{21} &= (2 - 3p_s)P_{e_1 i_0} P_{e_2 i_0}(P_{i_1 i_0} + P_{i_2 i_0}) \\
b_{22} &= (2p_s - 1)3P_{e_1 i_0} P_{e_2 i_0} P_{i_1 i_0} P_{i_2 i_0}.
\end{aligned} \tag{E4}$$

Appendix F: Computation of the spectrum of Lyapunov exponents

We calculate the largest Lyapunov exponent for the GCBM map $\vec{x}(t+1) = f(\vec{x}(t))$ Where we relabel the map as

$$\vec{x}_{p+1} = f(\vec{x}_p) \tag{F1}$$

Without loss of generality, we will assume p is the period of orbit such that

$$\vec{x}_p = \vec{x}_0 \text{ with } \vec{x}_p = f^p(\vec{x}_0) \tag{F2}$$

We will perturb in the direction of a tangent vector \vec{x}_0

$$\vec{x}_{p+1} = Df(\vec{x}_p) \cdot \vec{x}_p \tag{F3}$$

Where Df is the Jacobian Matrix.

Therefore, we can define

$$\vec{x}_p = Df^p(\vec{x}_0) \cdot \vec{x}_0, \tag{F4}$$

with

$$Df^p(\vec{x}_0) = Df^{p-1}(\vec{x}_{p-1}) \cdot Df^{p-2}(\vec{x}_{p-2}) \cdots Df(\vec{x}_0). \tag{F5}$$

We now can define the largest Lyapunov exponent as [56]

$$\lambda(\vec{x}_0) = \lim_{p \rightarrow \infty} \frac{1}{p} \ln \left(\frac{\|\vec{x}_p\|}{\|\vec{x}_0\|} \right) \tag{F6}$$

$$\lambda(\vec{x}_0) = \lim_{p \rightarrow \infty} \frac{1}{p} \ln \|Df^p(\vec{x}_0) \cdot \frac{\vec{x}_0}{\|\vec{x}_0\|}\|. \tag{F7}$$

To compute the Lyapunov spectrum $Df^p(\vec{x}_0)$ one may use the QR decomposition method of Ref. [50],

$$Df(\vec{x}_0) = Q_1 R_1, \tag{F8}$$

where Q_1 is an orthogonal matrix, and R_1 is an upper triangular with non-negative diagonal elements. The decomposition is unique if $Df(\vec{x}_0)$ is invertible. We define

$$Df^k = Df^{k-1}(\vec{x}_{k-1})Q_{k-1},$$

which can be decomposed

$$Df^k = Q_k R_k,$$

allowing us to write

$$Df^p(\vec{x}_0) = Q_p R_p \cdots R_1,$$

since the matrices Q_k s are orthogonal.

The diagonal elements $\lambda_{ii}(\vec{x}_0)^n$ of the upper right triangle of the product of $R_p \cdots R_1$ satisfy [57]

$$\lim_{n \rightarrow \infty} \frac{1}{n} \log \lambda_{ii}(\vec{x}_0)^n = \lambda_i(\vec{x}_0). \tag{F9}$$

[1] H. J. G. Gundersen, T. F. Bendsten, L. Korbo, N. Marcussen, A. Møller, K. Nielsen, J. R. Nyengaard, B. Pakkenberg, F. B. Sørensen, A. Vestby, and M. J. West, Some new, simple and efficient stereological methods and their use in pathologico-clinical research and diagnosis, *APMIS* **96**, 379 (1988), <https://onlinelibrary.wiley.com/doi/pdf/10.1111/j.1699-0463.1988.tb05320.x>.

[2] B. Pakkenberg, D. Pelvig, L. Marner, M. J. Bundgaard, H. J. G. Gundersen, J. R. Nyengaard, and L. Regeur, Aging and the human neocortex, *Experimental Gerontology* **38**, 95 (2003), proceedings of the 6th International Symposium on the Neurobiology and Neuroendocrinology of Aging.

[3] C. R. Olson and C. L. Colby, The organization of cognition, in *Principles of Neural Science, Fifth Edition*, edited by E. Kandel, J. Schwartz, T. Jessell, S. Siegelbaum, and A. Hudspeth (McGraw-Hill Education, New York, NY, 2014) p. 392.

[4] D. L. Meinecke and A. Peters, Gaba immunoreactive neurons in rat visual cortex, *Journal of Comparative Neurology* **261**, 388 (1987).

[5] C. C. Sadeh S, Inhibitory stabilization and cortical computation, *Nat Rev Neurosci* 10.1038/s41583-020-00390-z (2021).

[6] H. Wilson and J. Cowan, Excitatory and inhibitory interactions in localized populations of model neurons, *Biophysical journal* **12**, 1–24 (1972).

[7] S. Zapperi, K. B. Lauritsen, and H. E. Stanley, Self-organized branching processes: Mean-field theory for avalanches, *Phys. Rev. Lett.* **75**, 4071 (1995).

[8] J. X. de Carvalho and C. P. C. Prado, Self-organized criticality in the olami-feder-christensen model, *Phys. Rev. Lett.* **84**, 4006 (2000).

[9] C. Haldeman and J. M. Beggs, Critical branching captures activity in living neural networks and maximizes the number of metastable states, *Phys. Rev. Lett.* **94**, 058101 (2005).

[10] O. Kinouchi and M. Copelli, Optimal dynamical range of excitable networks at criticality, *Nature Physics* **2**, 348

(2006).

[11] S. Pajevic and D. Plenz, Efficient network reconstruction from dynamical cascades identifies small-world topology of neuronal avalanches, *PLOS Computational Biology* **5**, 1 (2009).

[12] C. T. Kello, Critical branching neural networks, *Psychological Review* **120**, 230 (2013).

[13] R. V. Williams-García, M. Moore, J. M. Beggs, and G. Ortiz, Quasicritical brain dynamics on a nonequilibrium widom line, *Physical Review E* **90**, 062714 (2014).

[14] R. C. López, V. Buendía, and M. A. Muñoz, Excitatory-inhibitory branching process: A parsimonious view of cortical asynchronous states, excitability, and criticality, *Physical Review Research* **4**, 10.1103/PhysRevResearch.4.L042027 (2022).

[15] J. M. Beggs and D. Plenz, Neuronal avalanches in neocortical circuits, *Journal of Neuroscience* **23**, 11167 (2003), <https://www.jneurosci.org/content/23/35/11167.full.pdf>.

[16] M. A. Muñoz, Colloquium: Criticality and dynamical scaling in living systems, *Rev. Mod. Phys.* **90**, 031001 (2018).

[17] L. J. Fosque, R. V. Williams-García, J. M. Beggs, and G. Ortiz, Evidence for quasicritical brain dynamics, *Phys. Rev. Lett.* **126**, 098101 (2021).

[18] H. C. Piuvezam, B. Marin, M. Copelli, and M. A. Muñoz, Unconventional criticality, scaling breakdown, and diverse universality classes in the wilson-cowan model of neural dynamics, *Phys. Rev. E* **108**, 034110 (2023).

[19] A. J. Fontenele, N. A. P. de Vasconcelos, T. Feliciano, L. A. A. Aguiar, C. Soares-Cunha, B. Coimbra, L. Dalla Porta, S. Ribeiro, A. J. a. Rodrigues, N. Sousa, P. V. Carelli, and M. Copelli, Criticality between cortical states, *Phys. Rev. Lett.* **122**, 208101 (2019).

[20] N. Friedman, S. Ito, B. A. W. Brinkman, M. Shimono, R. E. L. DeVille, K. A. Dahmen, J. M. Beggs, and T. C. Butler, Universal critical dynamics in high resolution neuronal avalanche data, *Phys. Rev. Lett.* **108**, 208102 (2012).

[21] W. L. Shew, H. Yang, S. Yu, R. Roy, and D. Plenz, Information capacity and transmission are maximized in balanced cortical networks with neuronal avalanches, *Journal of Neuroscience* **31**, 55 (2011).

[22] E. D. Fagerholm, G. Scott, W. L. Shew, C. Song, R. Leech, T. Knöpfel, and D. J. Sharp., Cortical entropy, mutual information and scale-free dynamics in waking mice, *Cerebral Cortex* **26**, 3945 (2016).

[23] A. J. Fontenele, N. A. D. Vasconcelos, T. Feliciano, L. A. Aguiar, C. Soares-Cunha, B. Coimbra, L. D. Porta, S. Ribeiro, A. J. Rodrigues, N. Sousa, P. V. Carelli, and M. Copelli, Criticality between cortical states, *Physical Review Letters* **122**, 10.1103/PhysRevLett.122.208101 (2019).

[24] M. G. Kitzbichler, M. L. Smith, S. R. Christensen, and E. Bullmore, Broadband criticality of human brain network synchronization, *PLOS Computational Biology* **5**, 1 (2009).

[25] V. Pasquale, P. Massobrio, L. Bologna, M. Chiappalone, and S. Martinoia, Self-organization and neuronal avalanches in networks of dissociated cortical neurons, *Neuroscience* **153**, 1354 (2008).

[26] T. Petermann, T. C. Thiagarajan, M. A. Lebedev, M. A. L. Nicolelis, D. R. Chialvo, and D. Plenz, Spontaneous cortical activity in awake monkeys composed of neuronal avalanches, *Proceedings of the National Academy of Sciences* **106**, 15921 (2009), <https://www.pnas.org/doi/pdf/10.1073/pnas.0904089106>.

[27] K. Binder, Finite size effects on phase transitions, *Ferroelectrics* **73**, 43 (1987).

[28] N. Weerawongphrom, J. B. Goetz, R. V. Williams-García, J. M. Beggs, and G. Ortiz, A minimal network of brain dynamics: Generalized cortical branching model, (2025).

[29] M. A. Moore, *Inhibition and Neural Optimization*, Ph.D. thesis, Indiana University (2018).

[30] A. Babloyantz, A. ; Destexhe, Low-dimensional chaos in an instance of epilepsy, *Proceedings of the National Academy of Sciences of the United States of America* **10.1073/pnas.83.10.3513** (1986).

[31] S. J. Iasemidis LD, Review: Chaos theory and epilepsy, *The Neuroscientist* **2**, 118 (1996).

[32] J. C. Sackellares, L. D. Iasemidis, D.-S. Shiao, R. L. Gilmore, and S. N. Roper, Epilepsy – when chaos fails, in *Chaos in Brain?* (World Scientific, 2000) pp. 112–133.

[33] S. Panahi, T. Shirzadian, M. Jalili, and S. Jafari, A new chaotic network model for epilepsy, *Applied Mathematics and Computation* **346**, 395 (2019).

[34] A. L. Hodgkin and A. F. Huxley, A quantitative description of membrane current and its application to conduction and excitation in nerve, *The Journal of Physiology* **117**, 500 (1952).

[35] A. Blot and B. Barbour, Ultra-rapid axon-axon ephaptic inhibition of cerebellar Purkinje cells by the pinceau, *Nature Neuroscience* **17**, 289 (2014).

[36] A. Bretto, *Hypergraph Theory: An Introduction*, Mathematical Engineering (Springer International Publishing, Heidelberg, 2013).

[37] T. C. B. Freeman, S. Durand, D. C. Kiper, and M. Carandini, Suppression without Inhibition in Visual Cortex, *Neuron* **35**, 759 (2002).

[38] N. Weerawongphrom, J. Goetz, R. V. Williams-García, J. M. Beggs, and G. Ortiz, A Minimal Network of Brain Dynamics: Generalized Cortical Branching Model (2025).

[39] L. J. Fosque, R. V. Williams-García, J. M. Beggs, and G. Ortiz, Evidence for Quasicritical Brain Dynamics, *Physical Review Letters* **126**, 098101 (2021).

[40] L. J. Fosque, A. Alipour, M. Zare, R. V. Williams-García, J. M. Beggs, and G. Ortiz, Quasicriticality explains variability of human neural dynamics across life span, *Frontiers in Computational Neuroscience* **16**, 10.3389/fncom.2022.1037550 (2022).

[41] F. K. Skinner, L. Zhang, J. L. P. Velazquez, and P. L. Carlen, Bursting in Inhibitory Interneuronal Networks: A Role for Gap-Junctional Coupling, *Journal of Neurophysiology* **81**, 1274 (1999).

[42] J. R. Gibson, M. Beierlein, and B. W. Connors, Two networks of electrically coupled inhibitory neurons in neocortex, *Nature* **402**, 75 (1999).

[43] H. Ye and S. Kaszuba, Inhibitory or excitatory? Optogenetic interrogation of the functional roles of GABAergic interneurons in epileptogenesis, *Journal of Biomedical Science* **24**, 93 (2017).

[44] W. Feller, *An Introduction to Probability Theory and Its Applications*, 3rd ed., Vol. 1 (John Wiley & Sons, New York, 1968).

[45] R. Hattori, K. V. Kuchibhotla, R. C. Froemke, and T. Komiyama, Functions and dysfunctions of neocortical inhibitory neuron subtypes, *Nature Neuroscience* **20**,

1199–1208 (2017).

[46] H. Nishimori and G. Ortiz, *Elements of Phase Transitions and Critical Phenomena* (Oxford University Press, 2010) https://academic.oup.com/book/8876/book-pdf/53437348/9780191035531_web.pdf.

[47] R. B. Griffiths, Thermodynamic functions for fluids and ferromagnets near the critical point, *Phys. Rev.* **158**, 176 (1967).

[48] R. V. Williams-García and S. Nicolis, Route to chaos in a branching model of neural network dynamics, *Chaos, Solitons & Fractals* **165**, 112739 (2022).

[49] A. Wolf, J. B. Swift, H. L. Swinney, and J. A. Vastano, Determining lyapunov exponents from a time series, *Physica D: Nonlinear Phenomena* **16**, 285 (1985).

[50] J. P. Eckmann and D. Ruelle, Ergodic theory of chaos and strange attractors, *Rev. Mod. Phys.* **57**, 617 (1985).

[51] J. Farmer, E. Ott, and J. A. Yorke, The dimension of chaotic attractors, *Physica D: Nonlinear Phenomena* **7**, 153 (1983).

[52] M. Sandri, Numerical calculation of lyapunov exponents, *Math. J.* **6**, 78 (1996).

[53] B. B. Mandelbrot, *Fractals: form, chance, and dimension* (W. H. Freeman, 1977).

[54] M. A. Whittington, R. D. Traub, and J. G. R. Jefferys, Synchronized oscillations in interneuron networks driven by metabotropic glutamate receptor activation, *Nature (London)* **373**, 612 (1995).

[55] P. Jiruska, M. de Curtis, J. G. R. Jefferys, C. A. Schevon, S. J. Schiff, and K. Schindler, Synchronization and desynchronization in epilepsy: controversies and hypotheses, *The Journal of Physiology* **591**, 787 (2013).

[56] P. Diamond, Phys 221a lecture notes - lyapunov exponents and their relation to entropy (2017), date of lecture: April 28, 2017.

[57] R. A. Johnson, K. J. Palmer, and G. R. Sell, Ergodic properties of linear dynamical systems, *SIAM Journal on Mathematical Analysis* **18**, 1 (1987), <https://doi.org/10.1137/0518001>.